This is a repository copy of *Wear induced ripplocation during dry sliding wear of TiC-based composite*.

White Rose Research Online URL for this paper:
http://eprints.whiterose.ac.uk/161181/

Version: Accepted Version

Article:

Magnus, C., Mostaed, A. orcid.org/0000-0002-2443-7819 and Rainforth, W.M. orcid.org/0000-0003-3898-0318 (2020) Wear induced ripplocation during dry sliding wear of TiC-based composite. Wear, 444-445. 203121. ISSN 0043-1648

https://doi.org/10.1016/j.wear.2019.203121

Article available under the terms of the CC-BY-NC-ND licence (https://creativecommons.org/licenses/by-nc-nd/4.0/).

Reuse

This article is distributed under the terms of the Creative Commons Attribution-NonCommercial-NoDerivs (CC BY-NC-ND) licence. This licence only allows you to download this work and share it with others as long as you credit the authors, but you can't change the article in any way or use it commercially. More information and the full terms of the licence here: https://creativecommons.org/licenses/

Takedown

If you consider content in White Rose Research Online to be in breach of UK law, please notify us by emailing eprints@whiterose.ac.uk including the URL of the record and the reason for the withdrawal request.

eprints@whiterose.ac.uk
https://eprints.whiterose.ac.uk/

Wear induced ripplocation during dry sliding wear of TiC-based composite

Carl Magnus[1,2], Ali Mostaed[1] and William M. Rainforth[1]

[1] Department of Materials Science and Engineering, The University of Sheffield, Mappin Street, Sheffield S1 3JD, UK.

[2] Anton Paar TriTec SA, Rue de la Gare 4, 2034 Peseux, Switzerland

Abstract

Monolithic TiC and TiC composite containing 30 and 50 mol% SiC were consolidated and synthesized using spark plasma sintering (SPS) without sintering aids. The as-sintered bulk samples microstructural and dry sliding room-temperature tribological properties against Al_2O_3 were characterized using X-ray diffraction (XRD), scanning electron microscopy (SEM), transmission electron microscopy (TEM) and Raman analyses. The role of mismatch in coefficient of thermal expansion (CTE) between TiC and SiC as well as cubic to hexagonal SiC phase transformation on the evolution of residual stresses in the composite was also investigated. The friction and wear properties of the monolithic TiC were superior to that of the composite with frictional heating-induced tribo-oxidation playing a dominant wear mechanism. The increase in friction and wear of the composite is attributed to wear-induced stress-relaxation of the previously trapped residual stresses in the composite leading to extensive ripplocation of the TiC grains and consequent SiC grain pull-outs. Herein, we report for the first time on wear-induced mechanical exfoliation of carbon, its subsequent decomposition to graphite and eventual deformation by micromechanism involving nucleation and propagation of ripples.

Keywords: Spark Plasma Sintering; High Temperature Ceramics; Dry Sliding Friction; Frictional Heating; Residual Stresses; Thermal Expansion; Ripplocations; Exfoliation

1. Introduction

The moderate fracture toughness of TiC and SiC ceramics which has limited their use in monolithic state, has led to the development of TiC-SiC composite system with improved fracture toughness [1, 2]. α-SiC has a hexagonal-closed-packed (HCP) crystallographic structure with three active slip systems. As a result, dislocation motion is impeded, thus fracture toughness is much lower as compared to metals. Addition of TiC particles into a SiC matrix or SiC particles into a TiC matrix has been found to yield promising composite systems with significantly improved strength and toughness [2, 3]. The increase in fracture toughness to about three or four times as large as that of monolithic states [4] has been associated predominantly with misfit of coefficient of thermal expansion (CTE) between the matrix and the second phase [5]. Misfit in thermal expansion introduces significant radial stresses at the phase boundaries and hoop compressive stresses inside the matrix. These stresses promote toughening mechanisms such as crack deflection, crack branching and stress-induced microcracking [5]. Furthermore, according to Wasche and Ajayi et al. [6, 7], the incorporation of particles of a second phase into monolithic ceramics can improve significantly their tribological behaviour, especially in unlubricated conditions. The resulting composite will enable the exploitation of the excellent wear properties of SiC whilst simultaneously benefitting from the high thermal expansion coefficient mismatch between TiC and SiC [8].

Currently, a comprehensive practical understanding of the role of residual stresses due to misfit in coefficient of thermal expansion between the matrix and the particle on wear behaviour is lacking, even though it has been well established theoretically that internal residual stresses can influence fracture and wear resistance of composites [9].

The objective of this work is to fabricate monolithic TiC and TiC-SiC composite systems by spark plasma sintering (SPS), and to investigate their dry sliding tribological behaviour as well as the role of stress-induced microcracking, due to mismatch in coefficient of thermal expansion between TiC and SiC, on the wear mechanism of the composite.

2. Experimental procedure

2.1. Ceramic material fabrication and characterization

Commercially available silicon carbide powder (cubic structure (β-SiC), 99.8 % purity, 1µm Alfa Aesar) and titanium carbide powder (99.5 % purity, 2 µm Alfa Aesar) were mixed according to Table 1 and ball milled in isopropanol using a 1.0 mm diameter zirconia ball at room temperature for 24 hours. The milled powder was then sieved using a 200 mesh sieve and subsequently synthesized by the spark plasma sintering (SPS) method. Details of the sample preparation and densification are summarized in Table 1.

Phase analysis of the SPSed polished unetched disc surfaces was carried out on a diffractometer (Bruker X/154 D2 Phaser, Germany) with Cu Kα radiation source using a step size of 0.02° and time per step 3 sec over a 2ϴ range from 5° - 80°. The microstructural evolution of the pristine and worn samples as well as toughening mechanisms were investigated by Vickers indentation (DuraScan G5, emco TEST), scanning electron microscopy (SEM) (FEI Inspect F50, The Netherlands) in conjuction with energy dispersive X-ray spectroscopy (EDS, Oxford

Instrument X-Max / Aztec Microanalysis, UK) and transmission electron microscopy (TEM), (FEI Tecnai Spirit / JEOL 3100Z R005 aberration corrected high-resolution TEM). TEM samples were prepared using a focused ion beam, (FIB), (FEI Helios NanoLab G3 UC, FEI company, The Netherlands) by lifting out sections from the pristine and worn surface which were then further thinned down using FIB for TEM analysis (Philips EM420 operating at 120 kV). Raman analyses was carried out ex-situ on the pristine and worn surfaces by employing a Si-calibrated inVia Raman spectrometer (Renishaw plc, UK) with an Ar laser (λ = 514.5 nm, laser output power 20 mW) and a 50x objective lens (spot size of 2 μm). Optical microscopy was used to further analyse the alumina balls after each test to investigate any possible material removal, oxidation and/or transfer materials from the bulk sample.

Table 1. Sample details and SPS sintering parameters

Powder precursor		***SPS sintering details***		
Bulk sample		***SPS environment***	***Holding time***	***Temperature***
Composition	***mol.%***	***gas***	***(min)***	***(°C)***
TiC	**100**	**Argon**	**15**	**2100**
TiC-SiC	**50-50**	**Argon**	**15**	**2100**
TiC-SiC	**70-30**	**Argon**	**15**	**2100**

Further details of the SPS synthesis and processing conditions are reported elsewhere [10].

2.2. Tribological behaviour

Unlubricated sliding wear tests were carried out using a pin on disk configuration (pin: Al_2O_3 (2 mm) and disk: monolithic TiC and TiC-SiC composite) in ambient conditions (25 °C and 38% RH) on a commercially available tribometer (TRB Anton Paar TriTec SA, Peseux, Switzerland). An Al_2O_3 ball was utilized as the counterface due to its relative inertness, as it would not be expected to react with the bulk sample and has been widely used in wear testing of TiC-based composites, and therefore the current results can better be compared to those in the literature. Tribological tests were conducted using a normal load 2 N, rotational speed 200 rpm (corresponding to a linear speed of ~ 0.12 m/s), at a sliding distance of 445 km for an hour. Schematic of the tribometer is shown in Figure 1. The frictional force and the normal load were continuously monitored by the load cell and the friction coefficient (CoF) was recorded in real time during the test. The specific wear rate was estimated by using Eq. (1) upon measuring the length and width of the wear track to determine the worn volume.

$$K = V/F_N X S_d \qquad (1)$$

Where K = specific wear rate (mm^3/Nm), V = wear volume (mm^3), F_N = load (N), and S_d = sliding distance (m), respectively.

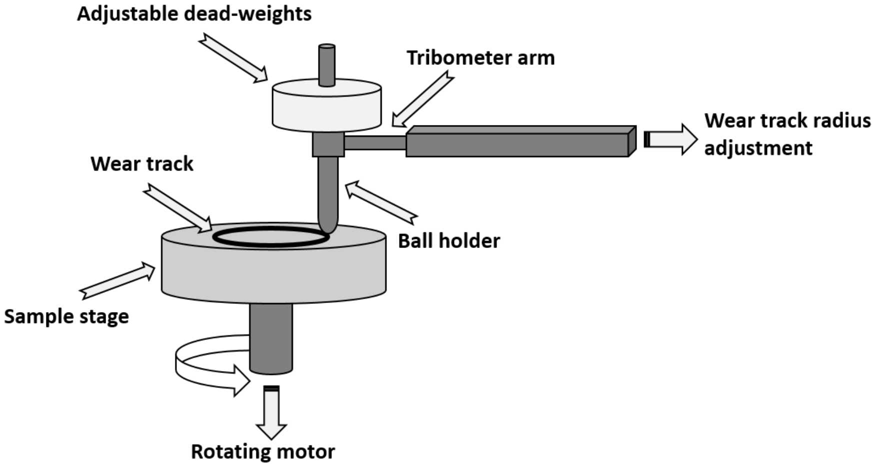

Fig. 1. Schematic of an Anton Paar tribometer employed for friction and wear test.

3. Results and Discussion

3.1. Phase analysis, densification, hardness and microstructure

The XRD patterns of the synthesized TiC-based ceramic composition are presented in Figure 2. As seen in the diffraction patterns, TiC and SiC phases were the only crystalline phases present indicating no solid solution reaction between the TiC and SiC phases. Also, as TiC and β-SiC are cubic in nature, their phases were somewhat indistinguishable owing to similar lattice parameters. However, some distinct peaks of α-SiC were detected due to possible phase transformation from $\beta \rightarrow \alpha$ – (SiC) at temperature above 1800 °C.

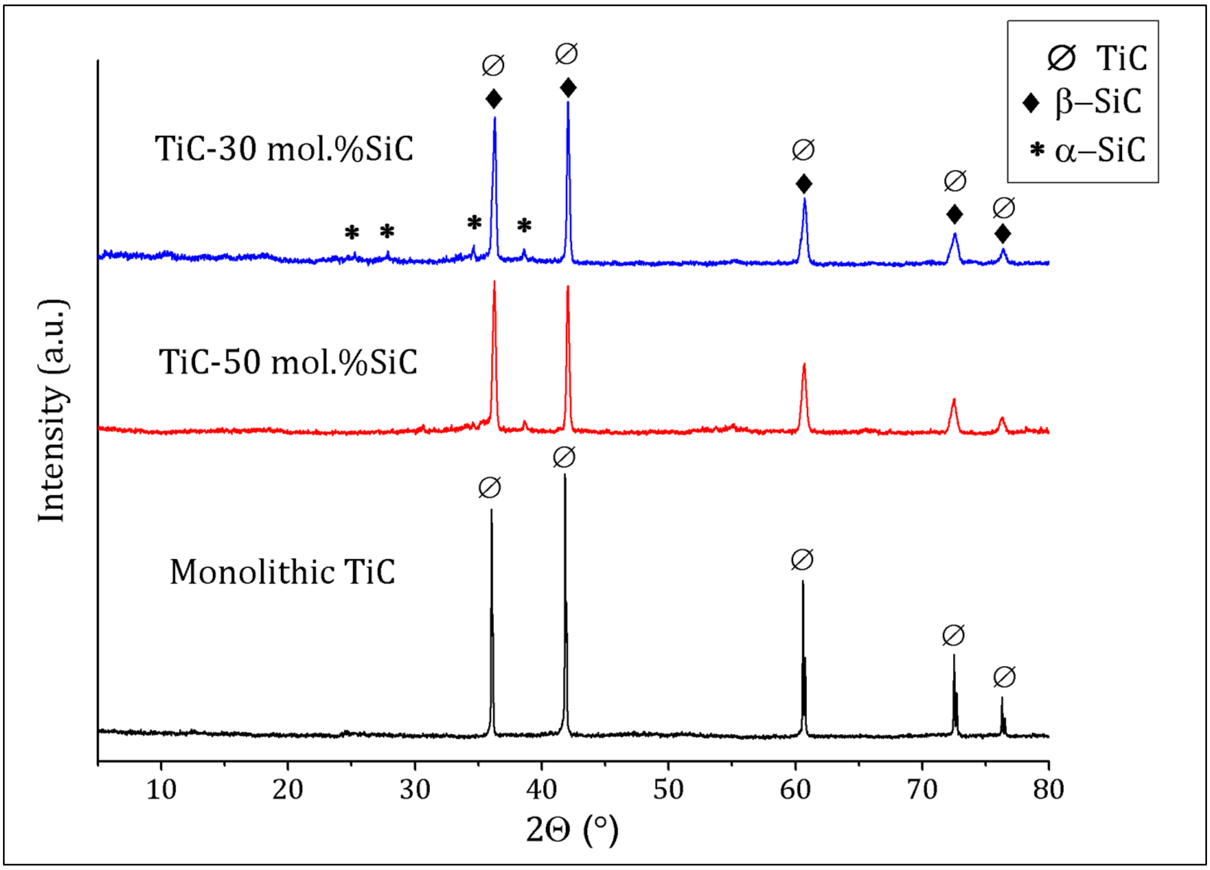

Fig. 2. X-ray diffraction patterns of the synthesized polished disc samples.

SPS produced fully dense specimens for both composition. The resulting SPS sintered compacts attained 98 % density for monolithic TiC, 99 % for TiC-50 mol.% SiC, and only 92 % for TiC-30 mol.% SiC, upon taking into account the theoretical densities of TiC (4.92 g/cm^3) and SiC (3.21g/cm^3), respectively. Vickers hardness measurement revealed that the composites possessed a slightly higher hardness than the monolithic TiC. For the measured values, the composites had the highest hardness ~ 3180 HV while the hardness of monolithic TiC was ~ 3000 HV. From the volumetric rule of mixtures, the expected hardness of the composite should be even higher [11]. However, owing to thermal expansion mismatch between SiC and TiC, the work of indentation may have been reduced due to the distribution of residual stresses in the composite [12].

The microstructure (Figures 3 and 4) of the TiC-SiC composite consist of two distinct phases of elongated particles of SiC (dark phase) homogeneously distributed in the TiC matrix (bright phase) as identified by EDS analysis (Figure 5). The presence of only two major phases is in agreement with the lack of solid solutions found in the SiC-TiC pseudo-binary system [13]. It is noteworthy to mention that one possible reason for SiC grain elongation may be possible β-

(SiC) $\xrightarrow{1800\,^{\circ}C}$ α-(SiC) phase transformation from cubic to hexagonal taking place during synthesis as explained elsewhere [14]. In comparison to the grain size of the monolithic TiC, the grain size of TiC in the TiC-SiC composite appears smaller. This can be attributed solely to the matrix grain-boundary pinning effect by the SiC particles during the sintering which inhibits the exaggerated TiC grain growth, consistent with observation reported elsewhere [15].

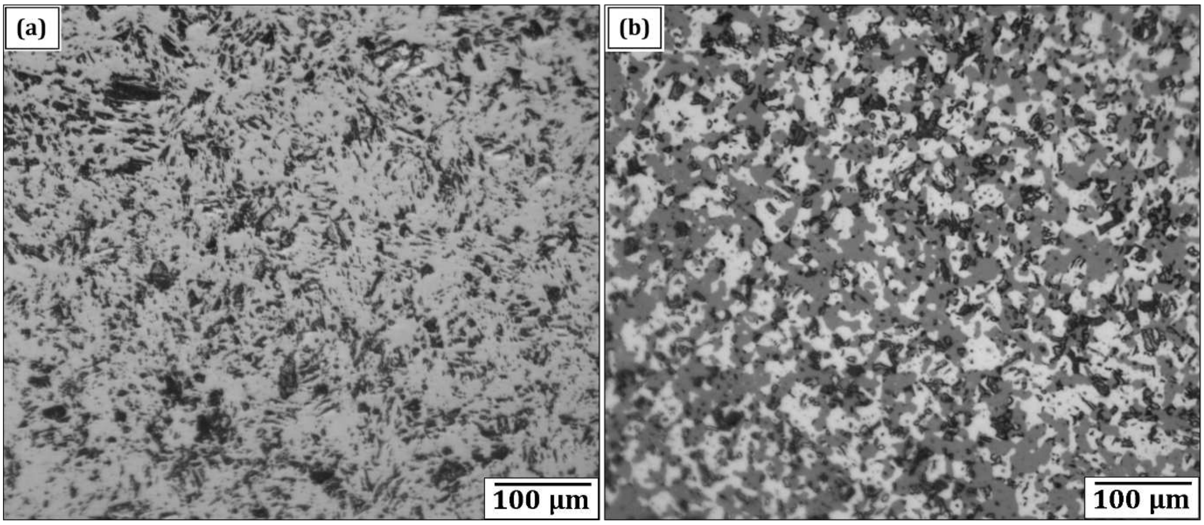

Fig. 3. Optical micrographs of the polished discs: (a) monolithic TiC and (b) TiC-50 mol.% SiC

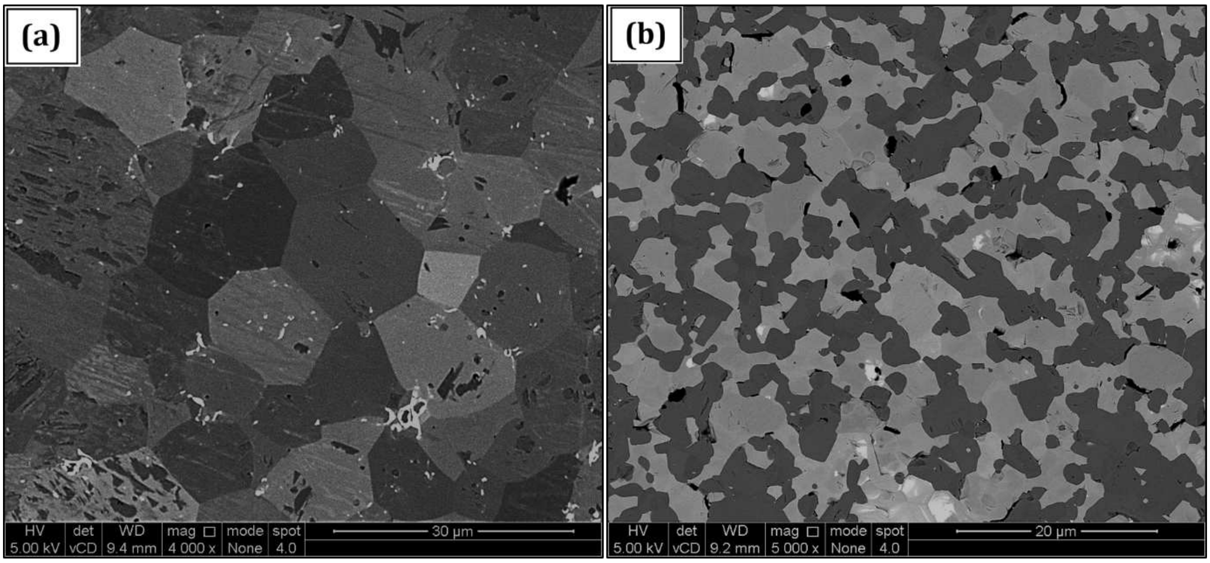

Fig. 4. SEM micrographs of SPSed polished unetched surfaces of the discs: (a) monolithic TiC and (b) TiC-50 mol.% SiC composite. Note: white bits left on samples microstructure are artefacts from colloidal silica.

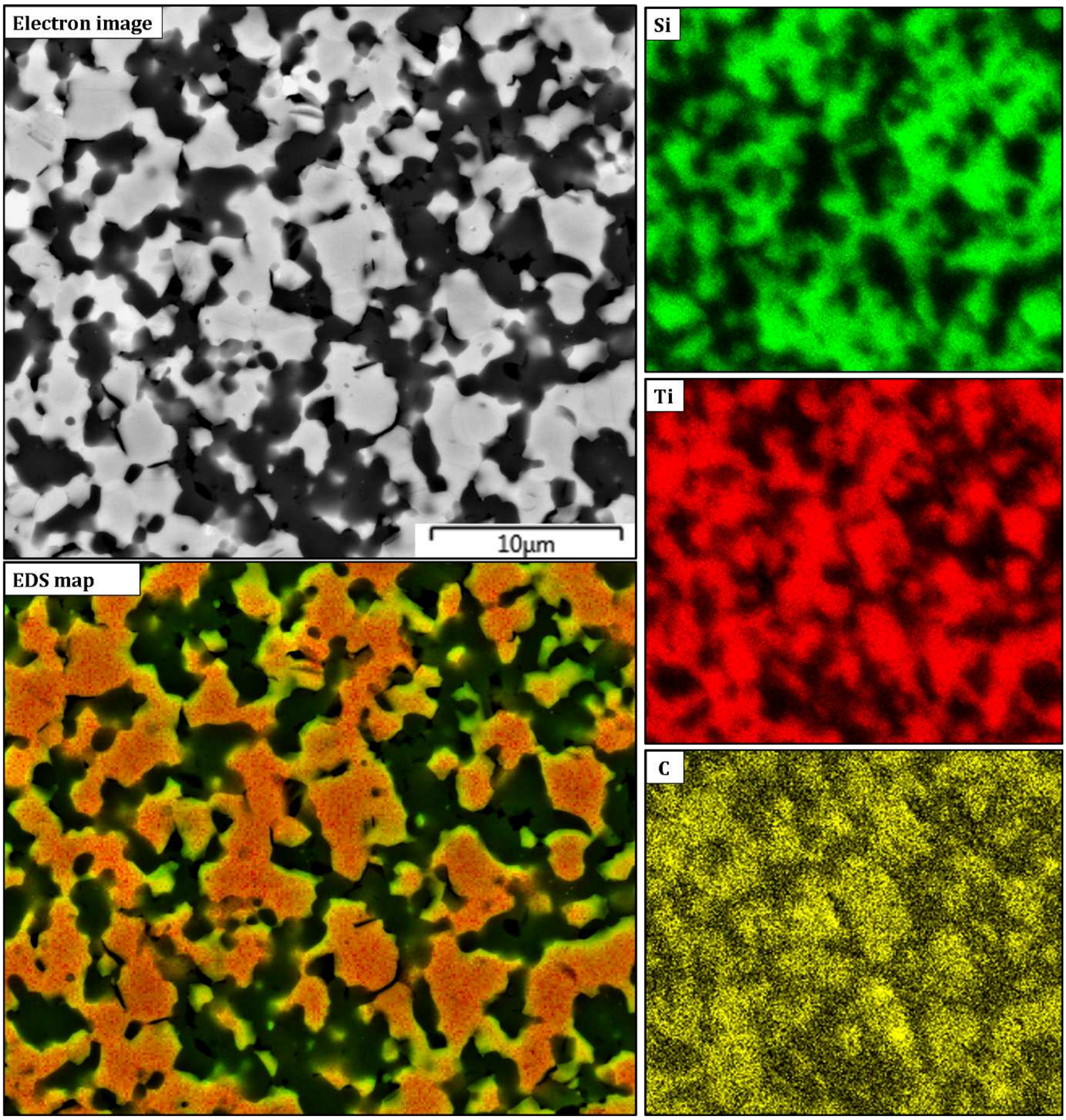

Fig. 5. EDS map analysis of the polished surface of the TiC-50 mol.%SiC showing elemental distribution. All scale bars 10 μm.

3.1.1. TEM of pristine surface of composite

Figure 6 shows TEM micrographs taken from the pristine surface of the TiC-50 mol.%SiC composite system. The TiC grain is essentially defect-free whilst profuse stacking fault can be seen in the SiC grain (1) (Fig. 6(a)). Higher magnifications of the SiC grain (1) further highlights the extent of the planar defect (stacking faults) which has been linked to the low stacking fault of energy in SiC (Fig. 6(b)). Evidence of partial dislocation (arrow in Fig.6(b)) can also be seen and represents the mechanism by which the growth of α-SiC nucleates (i.e., partial dislocation motion). This indicates that partial β→α phase transformation of SiC may have taken place during the SPS in consistent with the XRD analysis. To further verify the possible β→α phase transformation due to SPS above 1800 °C, TEM studies were done near the $<110>_{\beta}$ zone axis to reveal reciprocal lattice rows from which both the β and α patterns can be easily identified (i.e., extra spots are introduced into the β diffraction pattern due to the α polytype) as well as enabling the simultaneous visualization of the $[111]_{\beta}$ and $(0001)_{\alpha}$ planes edge-on. Lattice fringe image obtained from a partially transformed plate-like grain (2) is shown in Figure 6(c-f).

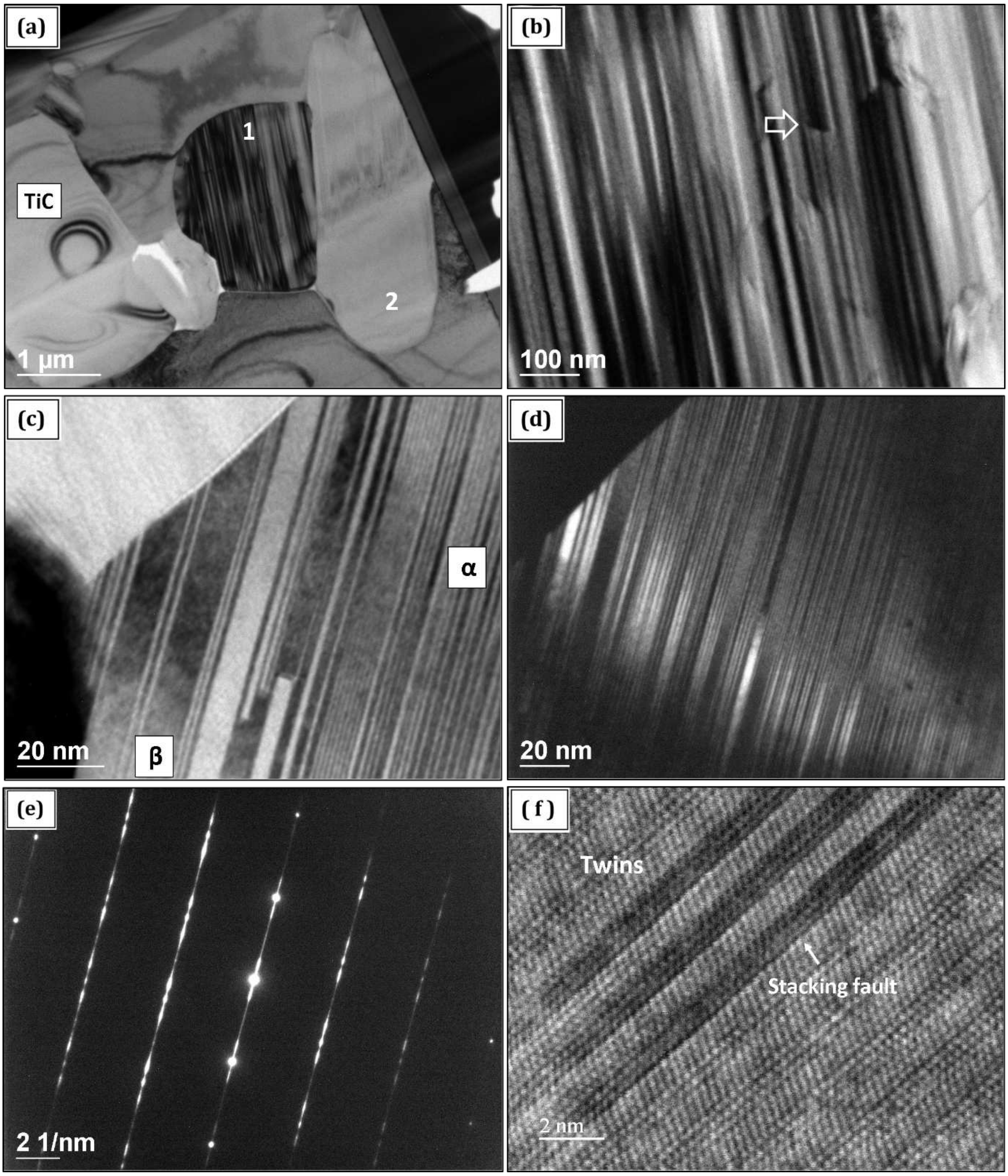

Fig. 6. (a-b) TEM bright-field images taken from the pristine surface of TiC-50 mol.% SiC composite, (c-d) Bright-field and Dark-field lattice fringe image of β/α interface region in a grain (1) which has been partially transformed with an array of β twins evident at the centre, (e) SAD patterns showing extra spot due to twins and (f) HRTEM image in the [110] zone axis evidencing twins and stacking faults.

3.2. Friction results

Figure 7 shows the characteristic evolution of the coefficient of friction with sliding time. For the TiC/Al_2O_3 couple subjected to sliding wear, the coefficient of friction was relatively stable throughout the entire test duration. This stable behaviour can be somewhat attributed to the formation of a triboreaction layer that appears stable as a function of time. On the other hand, the coefficients of friction of the TiC-SiC/Al_2O_3 tribocouples appear to be very unstable with repeated fluctuations. The reason for this might be due to instability of the triboreaction layer formed, or because the tribo-reaction layer formed is repeatedly worn off upon formation. Furthermore, TiC-SiC/Al_2O_3 tribocouples exhibited the highest steady state CoF values for the entire duration for the test conditions. The steady state mean value of CoF against Al_2O_3 was ~ 0.19 for TiC, ~ 0.35 for TiC-30 mol.%SiC, and ~ 0.39 for TiC-50 mol.%SiC composite, respectively.

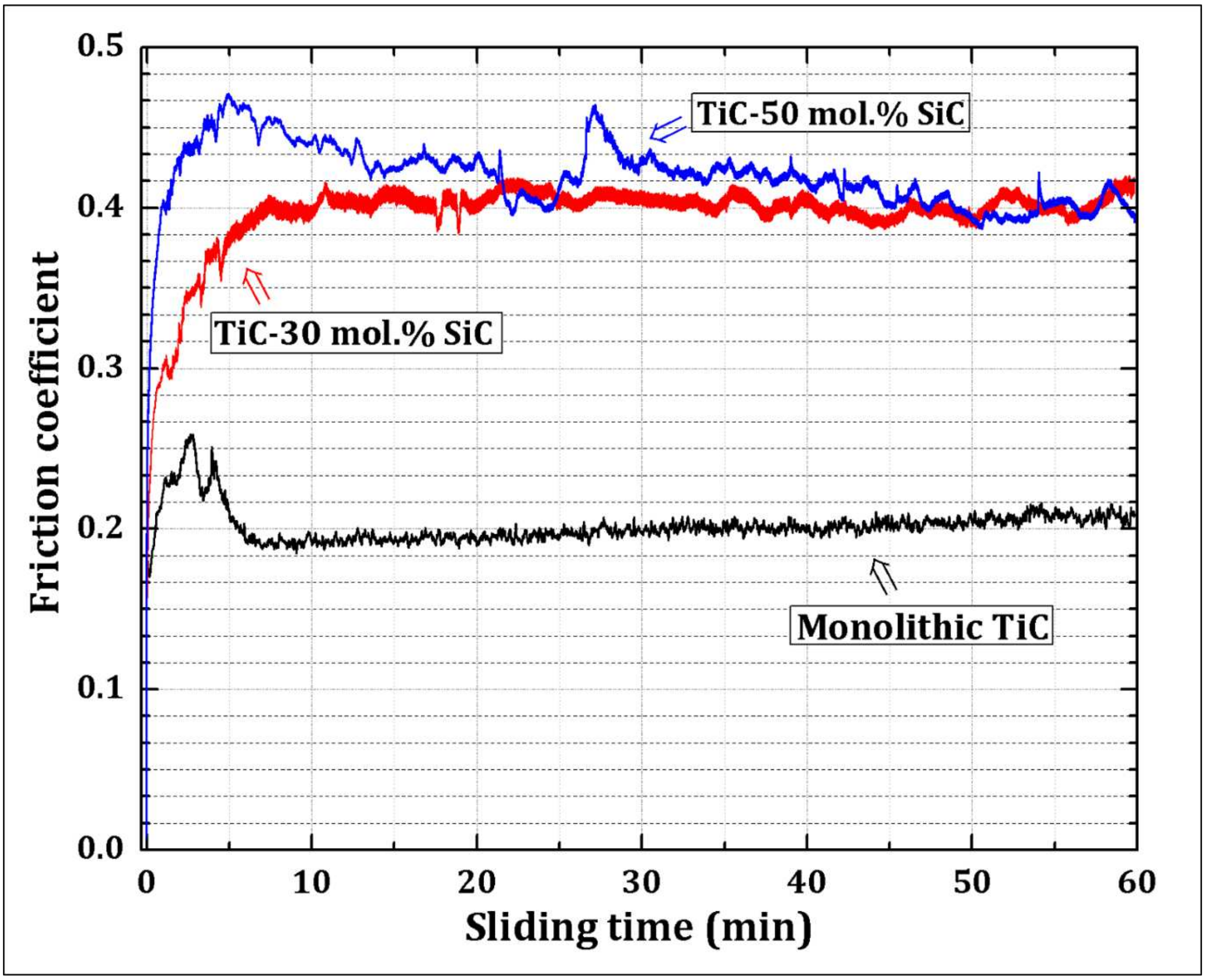

Fig. 7. Evolution of the friction coefficient with sliding time for rotational dry sliding contacts TiC/Al_2O_3 and TiC-SiC/Al_2O_3 composites, respectively at room temperature.

3.3. Wear results

The specific wear rate of TiC and TiC-SiC ceramic against Al_2O_3 ball is plotted in Figure 8. In general, the corresponding wear measurements reveal a correlated behaviour that is consistent with the friction curve. The specific wear rate is lower for TiC/Al_2O_3 tribocouple than for the TiC-SiC/Al_2O_3 indicating a major role of tribo-oxidation product in the wear mechanism. The TiC-SiC composite exhibited approximately 3 times more wear against Al_2O_3 as compared to monolithic TiC. It is believed that TiC reinforced with large amount of SiC would intrinsically exhibit higher fracture toughness that would lead to reduced mechanical fracture or grain pull-out during sliding wear [16]. However, the higher specific wear rate of the TiC-SiC composite as compared to monolithic TiC against Al_2O_3 would imply that fracture toughness was inactive or possibly inefficient possibly due to the role of thermal expansion mismatch between TiC. Almost comparable data on the friction and wear on a range of SiC-TiC composite system sliding against Al_2O_3 is presented elsewhere [17] albeit slight differences in testing parameters.

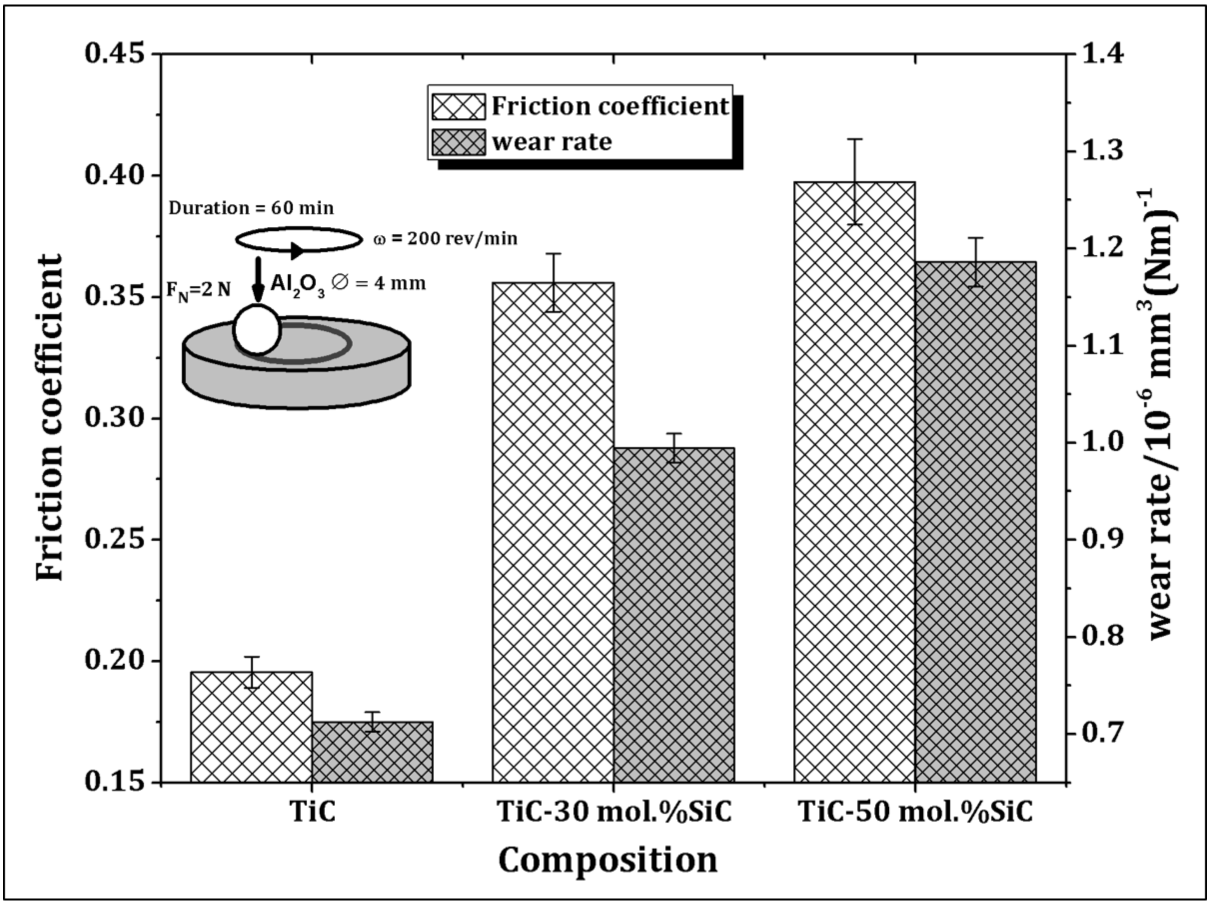

Fig. 8. Plot of wear rate and friction coefficient as a function of composition.

In the following and owing to the scope of this work, microstructural analyses will be focused essentially on the TiC-50 mol.%SiC.

3.4. Raman analysis

Since no observable Raman active vibration modes are present in stoichiometric TiC [8, 18], Raman spectra were collected from the β-SiC starting powder and bulk SPSed TiC-SiC composite as shown in Figure 9. The spectrum of the bulk TiC-SiC composite revealed characteristic peaks of the vibration mode of α-SiC indicating a phase transformation from cubic (β) → hexagonal (α) during SPS especially with the presence of α-SiC distinctive peak at 973 cm^{-1}, which is consistent with results obtained elsewhere [8, 19] as well as the TEM observation in Figure 6. The implication of such transformation is evident as observed in the microstructural evolution of the synthesized TiC-SiC composite where equiaxed β-SiC grains transforms to plate-like α-SiC grains.

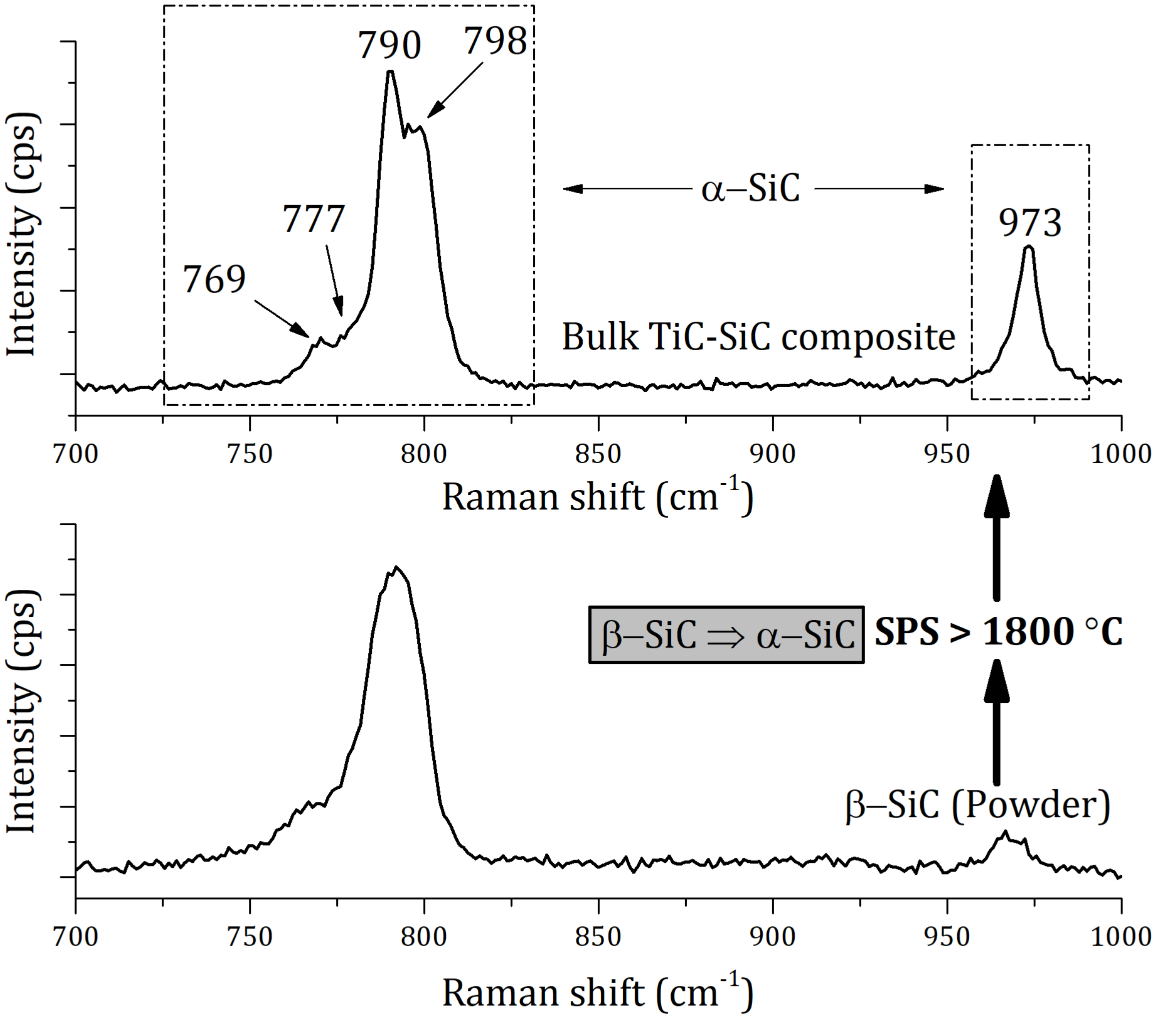

Fig. 9. Raman spectra of β-SiC powder and resulting SPSed bulk TiC-50 mol.% SiC composite pristine surface.

Raman analysis of the wear tracks of the TiC/Al_2O_3 and TiC-SiC/Al_2O_3 tribocouples are presented in Figures 10 and 11. In both cases the acquired Raman peaks correspond to vibrational modes of titanium oxide (typically rutile) and graphitic carbon upon comparing to literature data [20-22]. The formation of rutile would imply that anatase TiO_2, whose formation temperature is around ~ 500 °C, has been transformed into rutile as the temperature of the sliding surface increases due to frictional heating in accordance with [23];

$$\text{Anatase } (TiO_2) \xrightarrow{\sim 900\ ^\circ C} \text{Rutile } (TiO_2)$$

The Raman spectrum obtained from the composite shows lower intensity of TiO_2 peaks above the background in comparison to monolithic TiC. This could be attributed to the fact that the incorporation of SiC particles into the TiC matrix has reduced the amount of TiO_2 that can be formed due to frictional heating during dry sliding. On the other hand, the graphitic layer formed in the wear track of the composite appear to be much more intense compared to the background than the graphitic carbon peaks in the Raman spectrum of TiC/Al_2O_3 wear track. The reason for this is not fully understood but it is conceivable that SiC is responsible for the increased graphitization of the TiC-SiC/Al_2O_3 tribocouples' sliding interface.

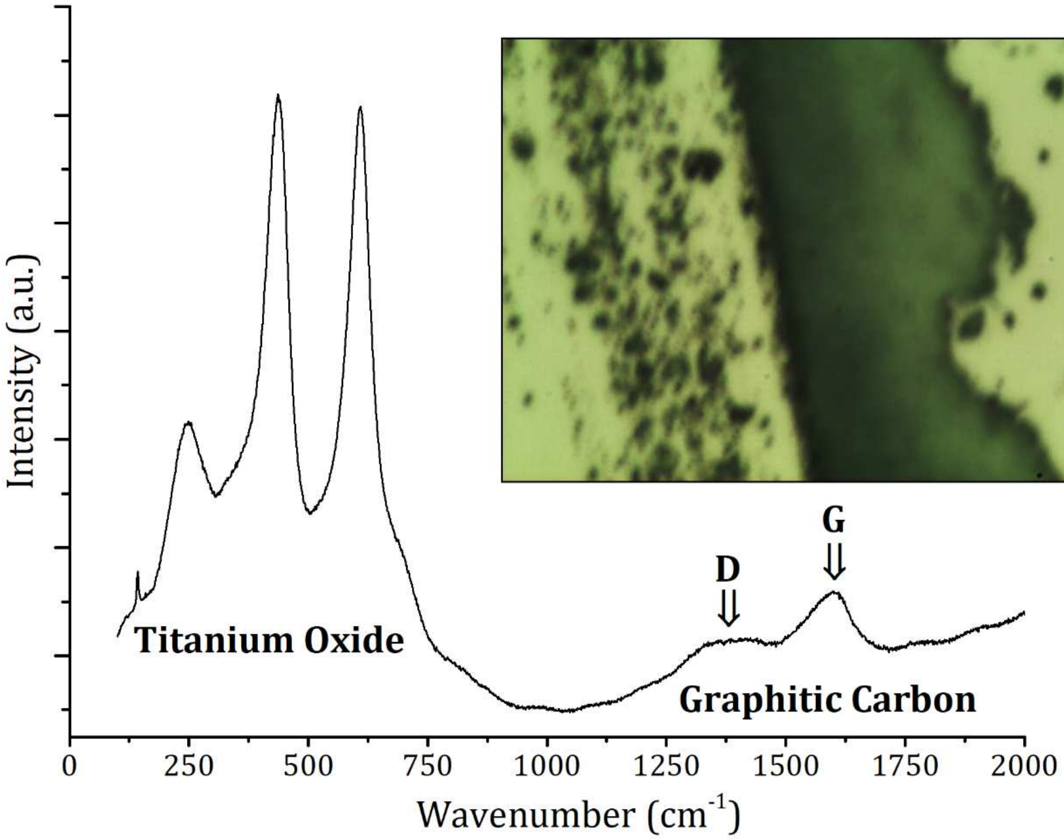

Fig. 10. Raman spectra obtained inside in the wear track of TiC/Al_2O_3 tribocouple. Inset is a micrograph of the sliding surface tribofilm where point spectrum was acquired.

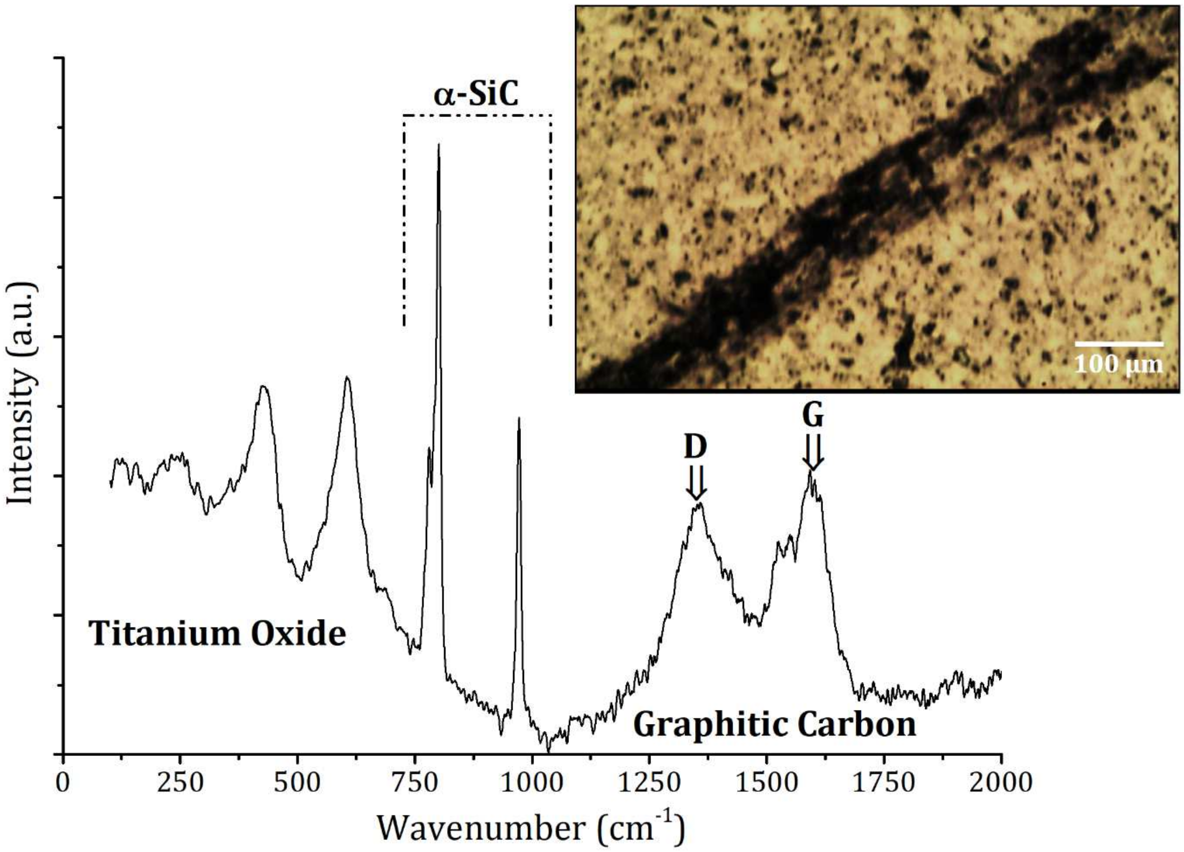

Fig. 11. Raman spectra obtained inside in the wear track of TiC-50 mol.% SiC/Al_2O_3 tribocouple.

3.5. Post-mortem SEM analysis of wear track

Post mortem SEM and EDS assessments of the sliding interface of TiC/Al_2O_3 tribocouples are presented in Figures 12 and 13. The wear scar of the TiC/Al_2O_3 sliding surface appears to be moderately damaged with grain fracture and subsequent pulverization evident. Sharp wear grooves can also be seen along the wear track. Tribofilms appear not to be visible inside the wear track even though Raman analysis revealed the evolution of tribo-oxidation products. A major reason for non-existence of tribofilms might be that they have been worn off and/or incorporated and mixed with the wear debris. Nonetheless, EDX analysis of the fractured surface (Fig. 12(b)) presented in Figure 13 is quite consistent with Raman analysis in finding oxides on the surface.

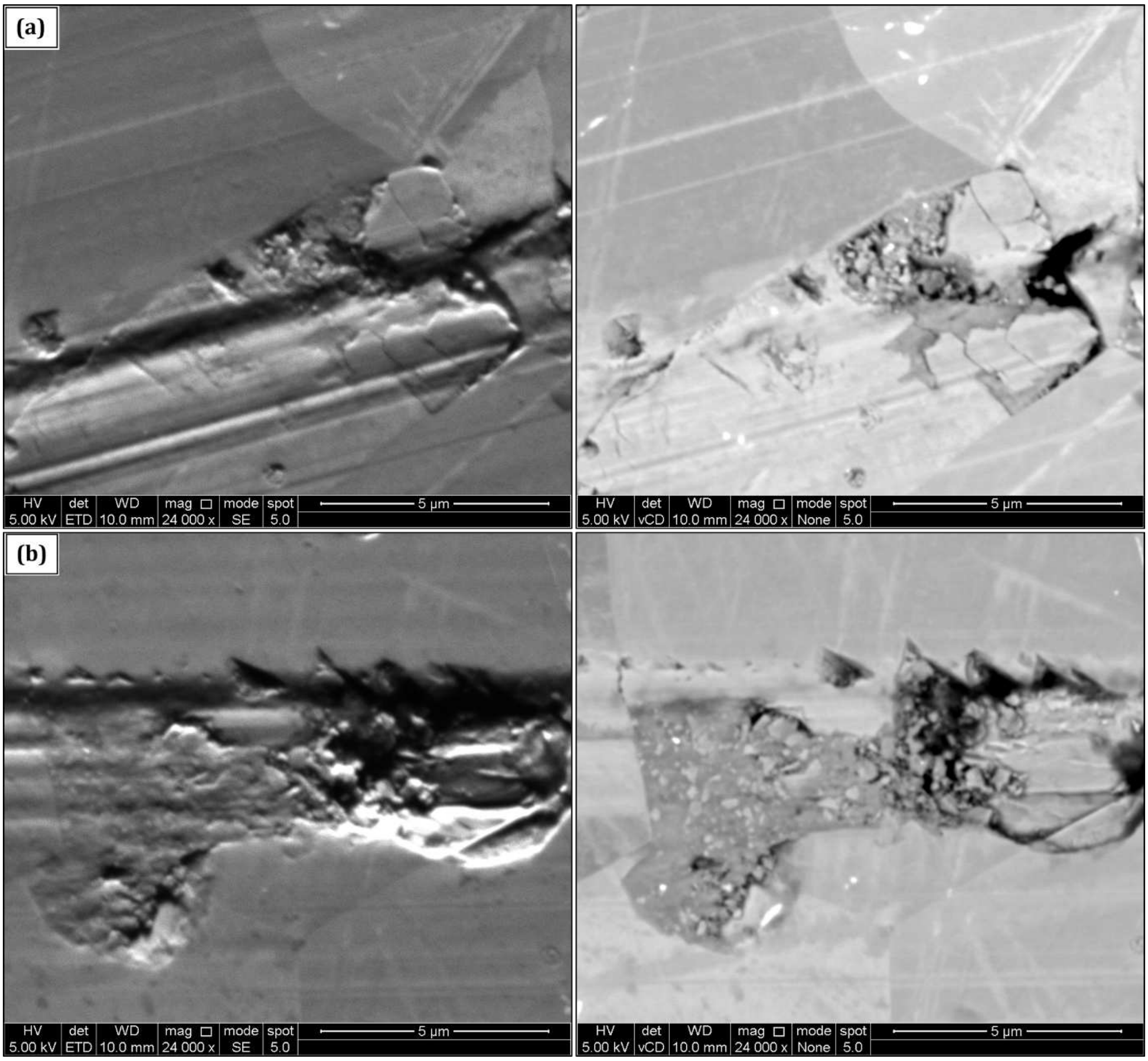

Fig. 12. Post-mortem topographical (SE-BSE) SEM micrographs of the sliding surface of TiC/Al_2O_3 tribocouple.

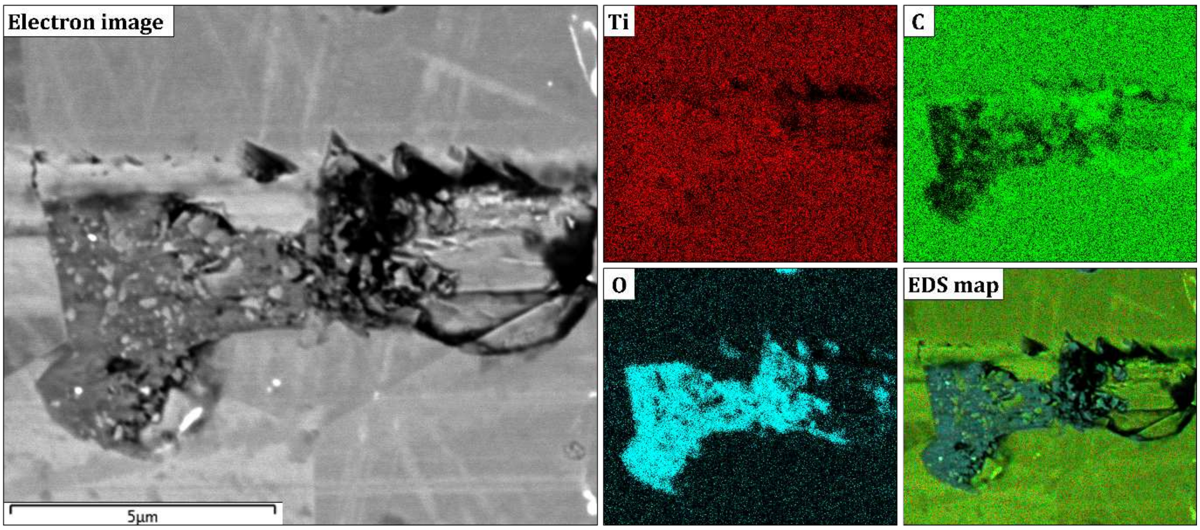

Fig. 13. EDX elemental map analysis taken at the sliding surface of TiC/Al_2O_3 tribocouple.

The sliding surface of the TiC-SiC/Al_2O_3 tribocouple on the other hand is presented in Figure 14. Severe wear grooves (Fig.14(a)) running parallel across the wear track and fracture of the grains (Fig.14(c-d)) are observed. In addition, tribofilms (Fig.14(b)) as well as extensive rippling of the TiC grains (Fig.14(e-f)) are evident in the wear track. The reason for the rippled TiC grains is not fully clear but might have been linked to the thermal expansion mismatch between TiC and SiC. In general the observed grain damage is surprising given the high content of easy-shearing graphitic material observed in the wear track of TiC-SiC/Al_2O_3 tribocouples using Raman analysis. Nonetheless, the observed microstructural damage seems to explain the higher coefficient of friction measured for the TiC-SiC/Al_2O_3 tribocouples as compared to monolithic TiC.

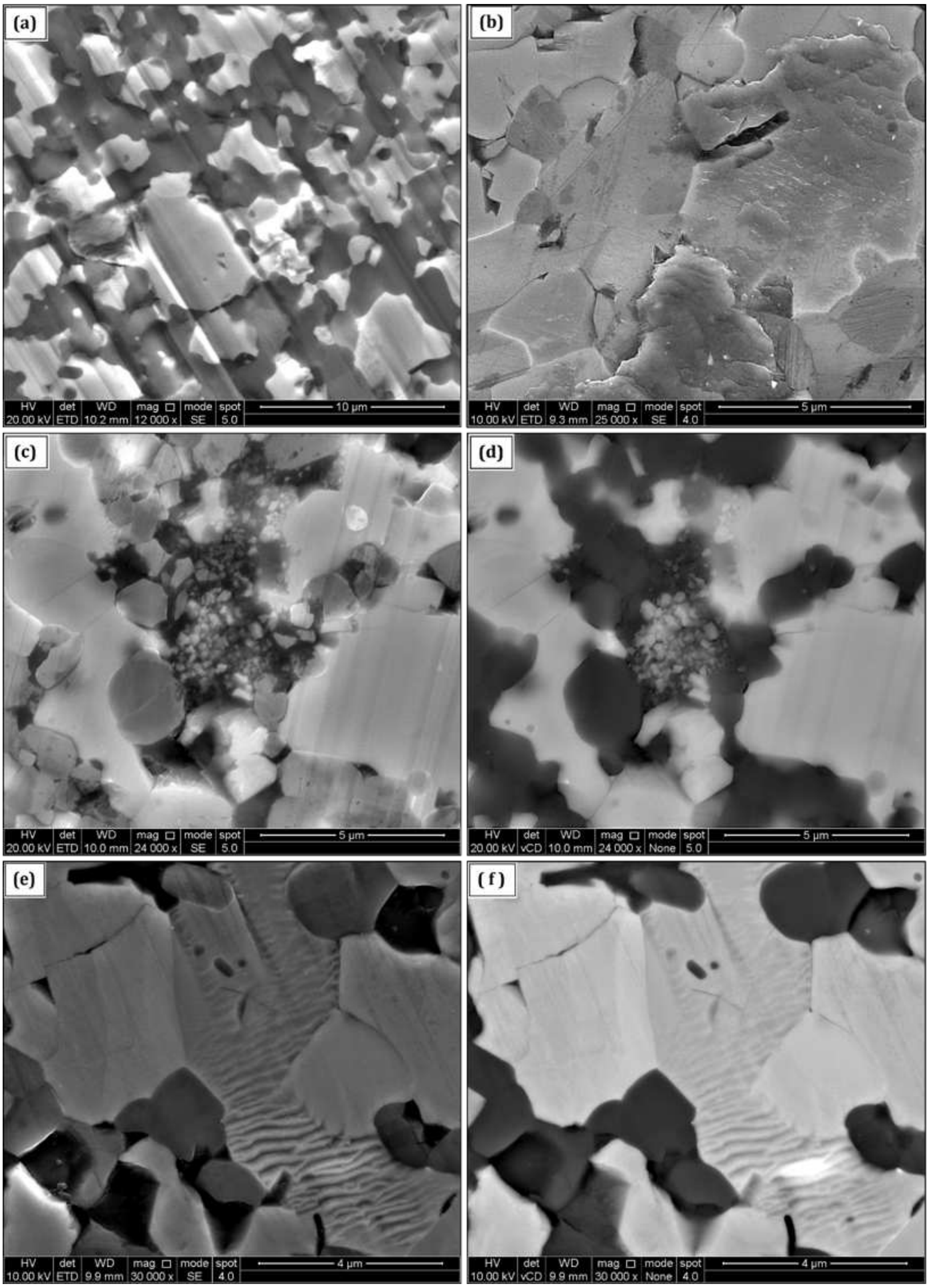

Fig. 14. Post-mortem topographical SEM micrographs of the contacting surface of the TiC-50 mol.% SiC/Al_2O_3 tribocouple. Note (a and b) are SE-images whilst (b-c) and (e-f) are SE-images and their corresponding backscattered (BSE) images.

Figure 15 shows the comparative SEM-EDS elemental map analyses of an area inside the wear track of the TiC-50 mol.%SiC composite system. Preferential oxygen concentration around the TiC region can be observed which suggests possible TiO_2 oxide formation in consistent with the Raman analysis. However, it is difficult using EDS analysis to distinguish between the intrinsic carbon content from the bulk sample composition and the graphitic layer formed due to the tribochemical reaction.

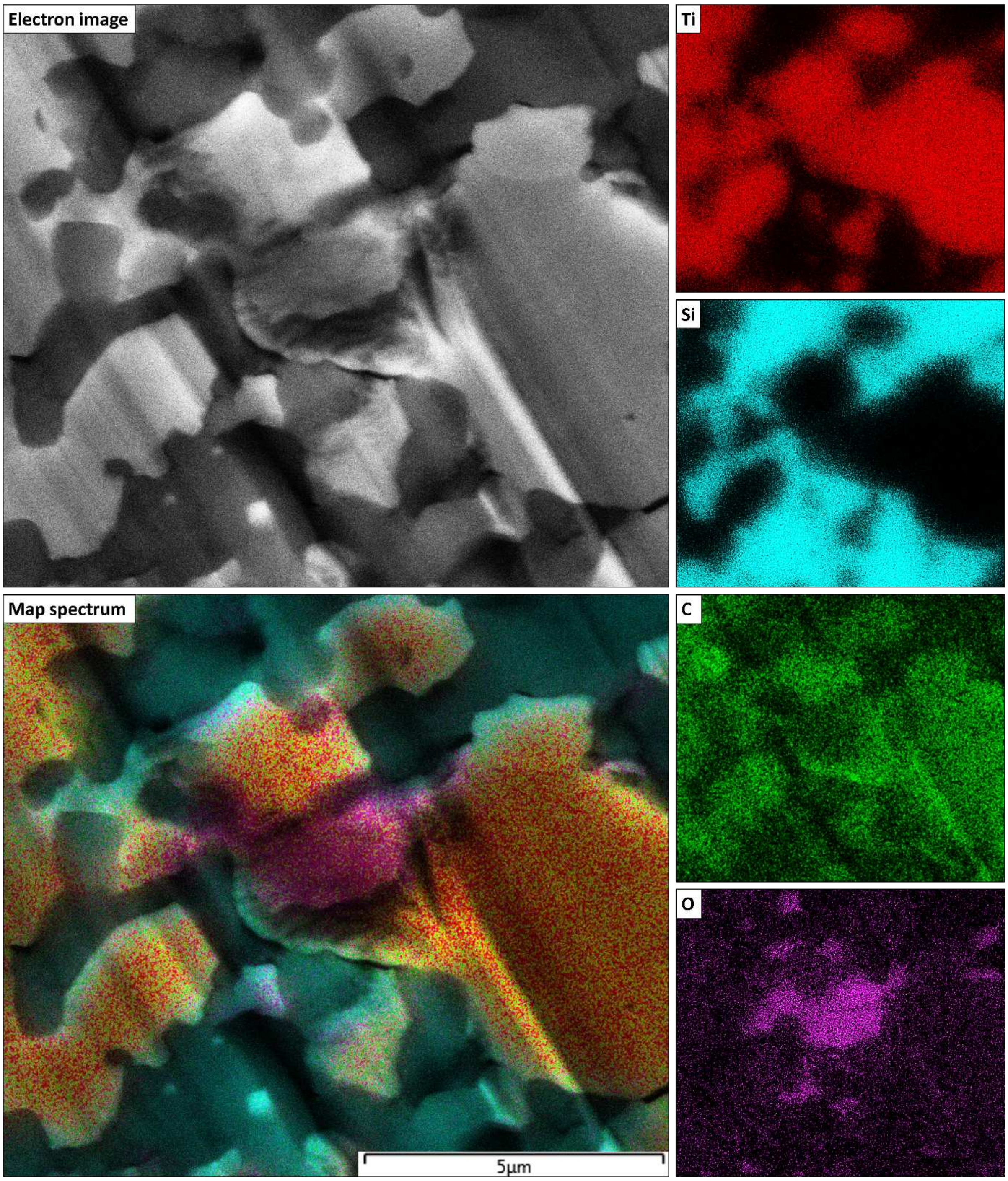

Fig. 15. EDS elemental map analysis taken from the worn surface of the TiC-50 mol.%SiC composite.

To further understand the wear mechanism, the surface of the alumina balls were analysed after each test. Analysis of the alumina ball after dry sliding against monolithic TiC (Fig. 16) showed some transfer film on the ball as well as minor wear of the ball surface. The alumina ball surface after dry sliding against TiC-50 mol.%SiC (Fig. 17) also showed that some wear debris was transferred to the balls surface. In addition, the ball surface appeared relatively rough and covered with compacted oxidized wear debris and/or smeared tribofilm. Wear grooves parallel to the sliding direction were also visible on the balls' surfaces. It appears that debris accumulation on the surface of the ball grows as a function of time and ultimately enough debris is entrapped between the ball and the disc which then acts as a load bearing third-body. This will result in increase in contact force due to point contacts with particles and thus brings about fluctuations in friction behaviour and increase in friction coefficient.

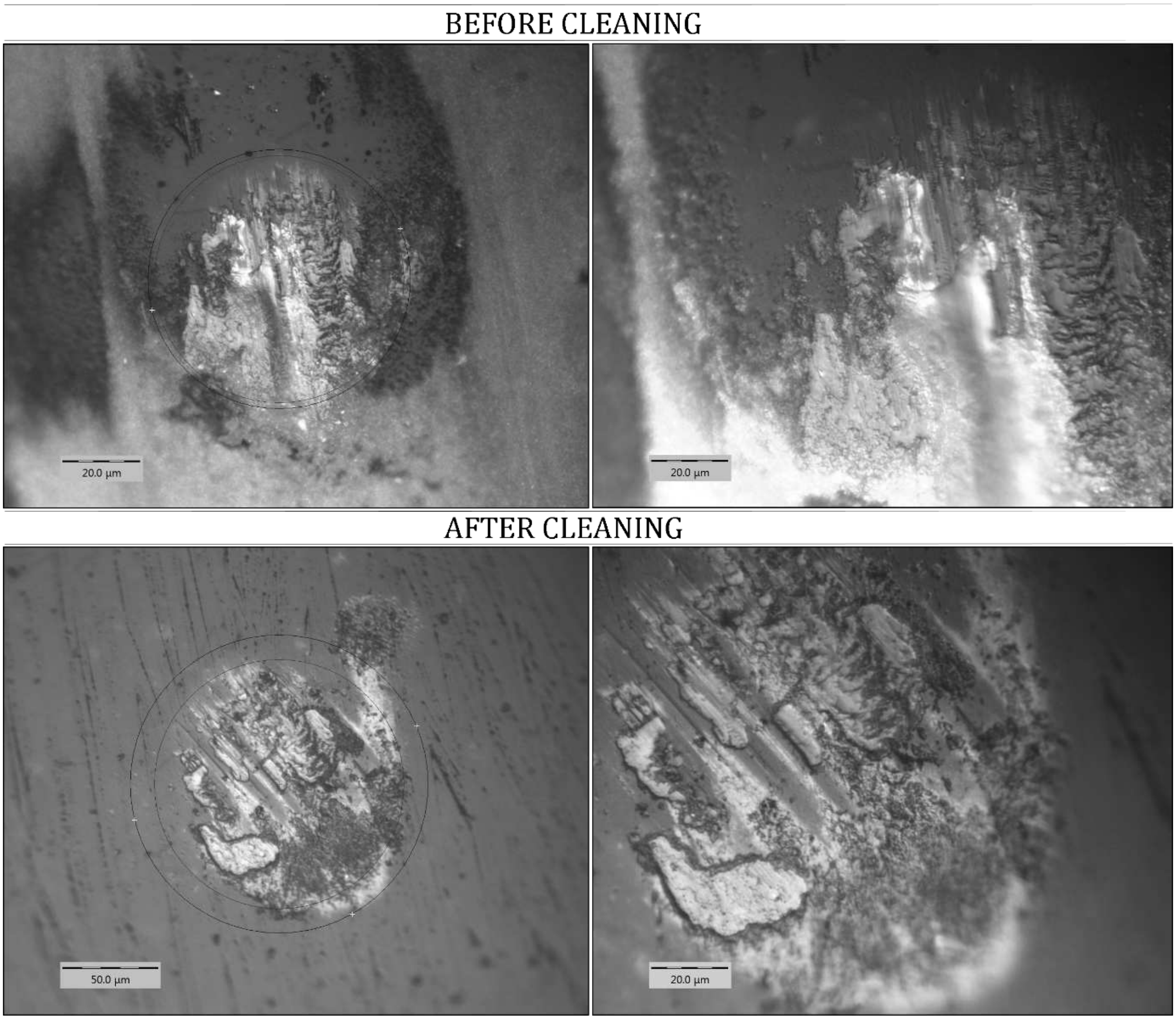

Fig. 16. Optical images of the alumina ball surface after dry sliding against monolithic TiC.

BEFORE CLEANING

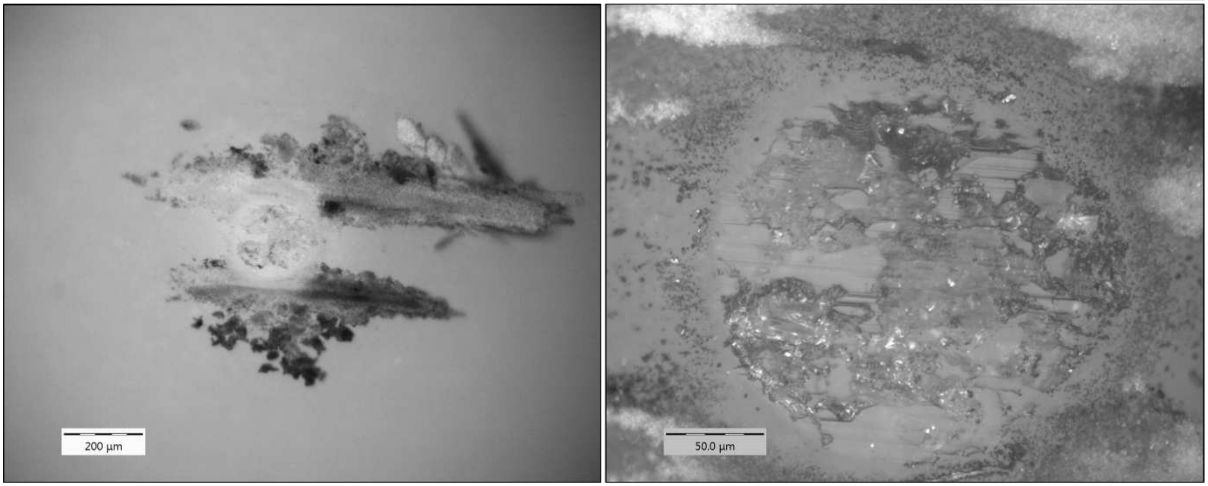

AFTER CLEANING

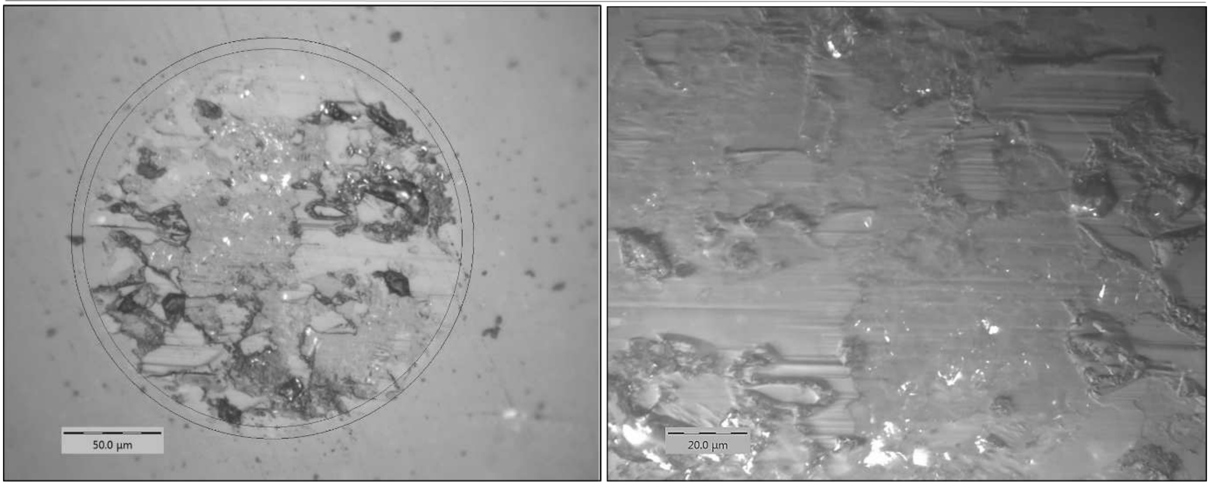

Fig. 17. Optical images of the alumina ball surface after dry sliding against TiC-50 mol.%SiC.

3.6. Toughening mechanism

As seen in Figure 4, the presence of SiC particles in the TiC matrix inhibited the exaggerated grain growth of the TiC grains, and as a consequence, toughening mechanisms will be initiated according to [1, 24, 25]. Furthermore, in addition to the SiC pinning toughening effect, the mismatch in coefficient of thermal expansion between TiC and SiC will introduce an additional toughening mechanism [1, 26]. This is because the thermal expansion coefficient of TiC is larger than that of SiC ($\alpha_{SiC} \approx 5.3 \times 10^{-6}$ °C^{-1} and $\alpha_{TiC} \approx 7.4 \times 10^{-6}$ °C^{-1}, respectively [27]) and as a consequence hydrostatic compressive stress will be generated within the SiC grains [25]. At the same time, radial compressive stress and tangential tensile stress will be generated in the TiC matrix around the SiC particles [1, 25]. Thus, if SiC is located on a crack extension plane, the crack will preferentially first reach the boundary of the TiC and SiC grains, as the surface energy of the SiC grains is larger than the interface surface fracture energy of the

TiC/SiC interface [28]. As a result the crack will bypass the TiC matrix and SiC particle and instead propagate along the TiC/SiC interface [28]. However, occasionally the crack will propagate through the particle if they possess irregular shape and size [25, 28]. Figure 18 is a typical SEM micrograph of the trajectories of indentation cracks in the TiC-50 mol.% SiC composite. Energy absorbing toughening mechanisms such as crack deflection, crack branching and crack bridging are evident.

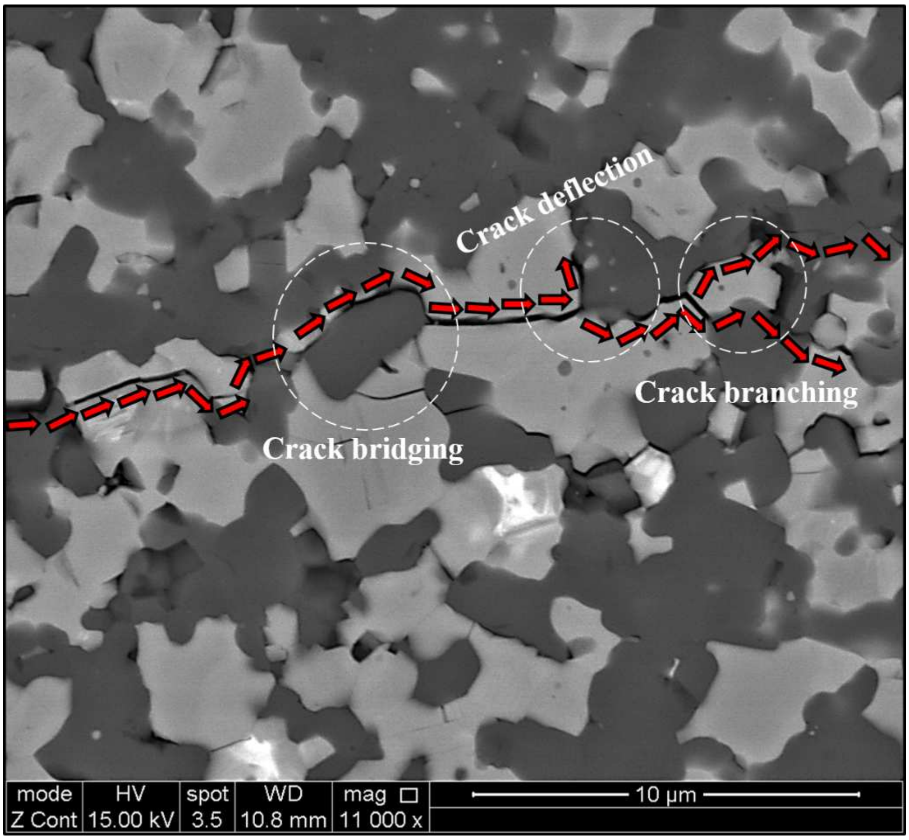

Fig. 18. Toughening mechanism in TiC-SiC composite with crack propagating preferentially along the grain boundary and occasionally deviating into the TiC and SiC grains.

3.7. Thermal expansion mismatch and residual stress

It has been well established that particulate composites generally contain inherent residual stresses by virtue of the mismatch in thermal expansion between the matrix and the particles, which is likely to initiate spontaneous microcracking when the second phase particle size attains a critical value [29, 30]. SEM investigation of the as-synthesized SPSed composite showed evidence of neither microcracking nor fracture which would imply that the second phase SiC particle size distribution is below the critical size where spontaneous microcracking is initiated [30]. The absence of cracks implied that stresses due to thermal expansion mismatch have not been relieved, thus strain due to thermal cycling during the synthesis is retained in the composite (i.e., stress relaxation has not occurred). SEM observation of the composite wear track, in contrast to the worn surface of the monolithic TiC, revealed evolution of stress relaxation upon dry sliding contact. The TiC grains in the TiC-SiC composite is observed to have undergone severe rippling preferentially (Fig. 19) with no rippling behaviour observed in the SiC grains. This strongly suggests that stress due to thermal mismatch has been relieved (i.e., stress-relaxation) during the wear process. According to Luan et al. [31], residual stress trapped in composites could be relaxed significantly when there is a subsequent mechanical loading that causes superposition of the applied stress and residual stress via stress-induced microcracking [29, 32]. Such consequent stress-induced microcracking is expected to shield a propagating crack by the release of residual stress around the applied load [33, 34] i.e., toughening. However, the beneficial compressive stresses appear to have been worn off during the wear process, rendering toughening mechanisms such thermal residual toughening and microcracking inactive or inefficient against future loading, as only detrimental tensile stresses are left behind in the matrix that promotes severe rippling and consequent microcracking of the surrounding grains.

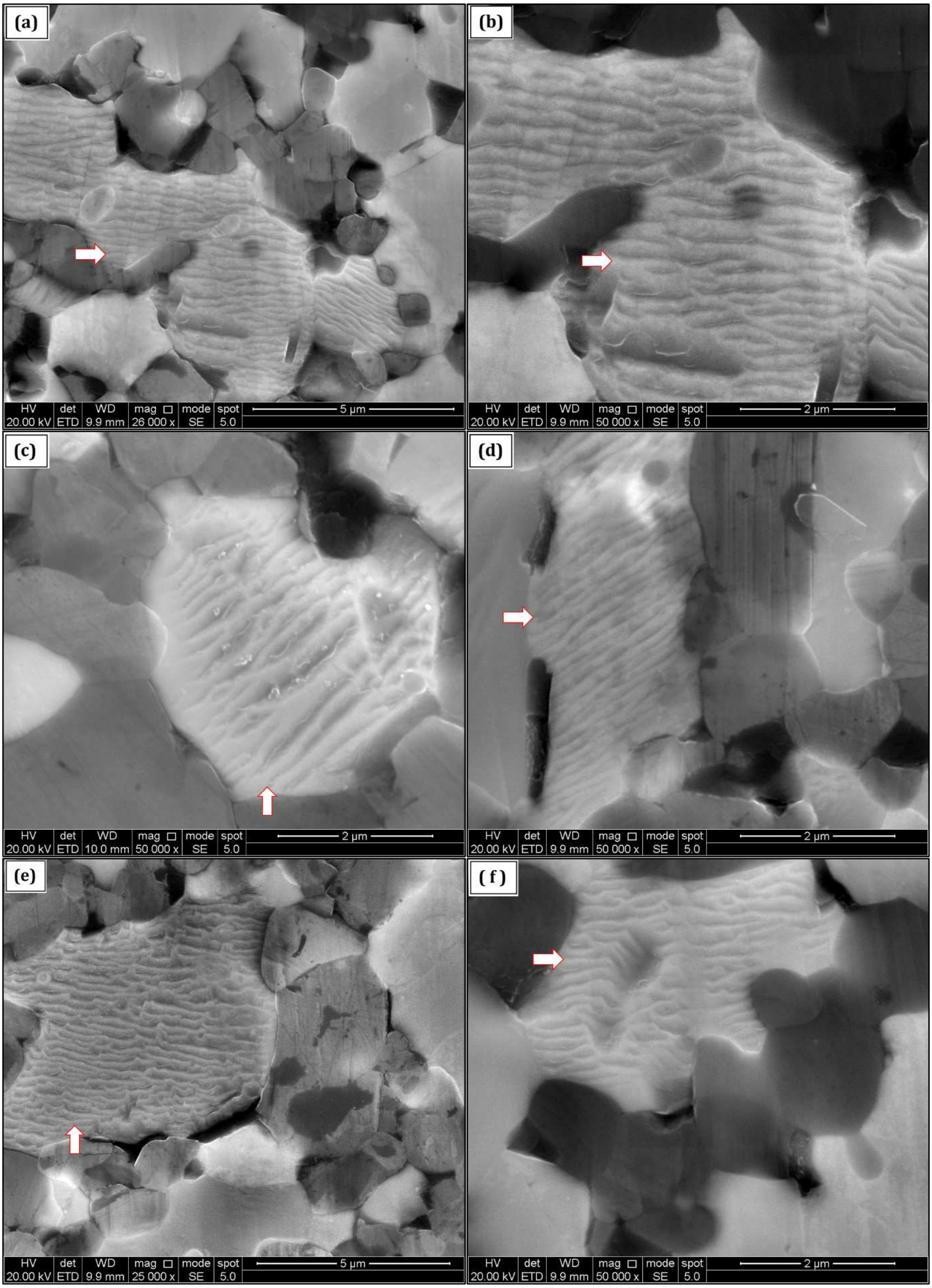

Fig. 19. SEM micrographs of the worn surface of the TiC-50 mol.%SiC composite showing evidence of extensive TiC grain ripplocation upon stress-relaxation. Note: (b) is a higher magnification of a section in (a).

In order to further provide detailed overview of the buckled section, 3D data were obtained from SEM images of the buckled section by employing 3D –image analytic software (MountainsMap® SEM Topo, Digital Surf, France) to reconstruct the backscatter SEM image. From the SEM 3D reconstruction (Fig. 20), extensive SiC grain pull-outs and fracture can be seen around the rippled TiC grains. It appears that the SiC grains are pulled out due to TiC grain ripple formation nearby and subsequently pulverized due to the contact load. Whilst the TiC grains on the other hand undergo micro and macro-fracture due to residual stress relaxation.

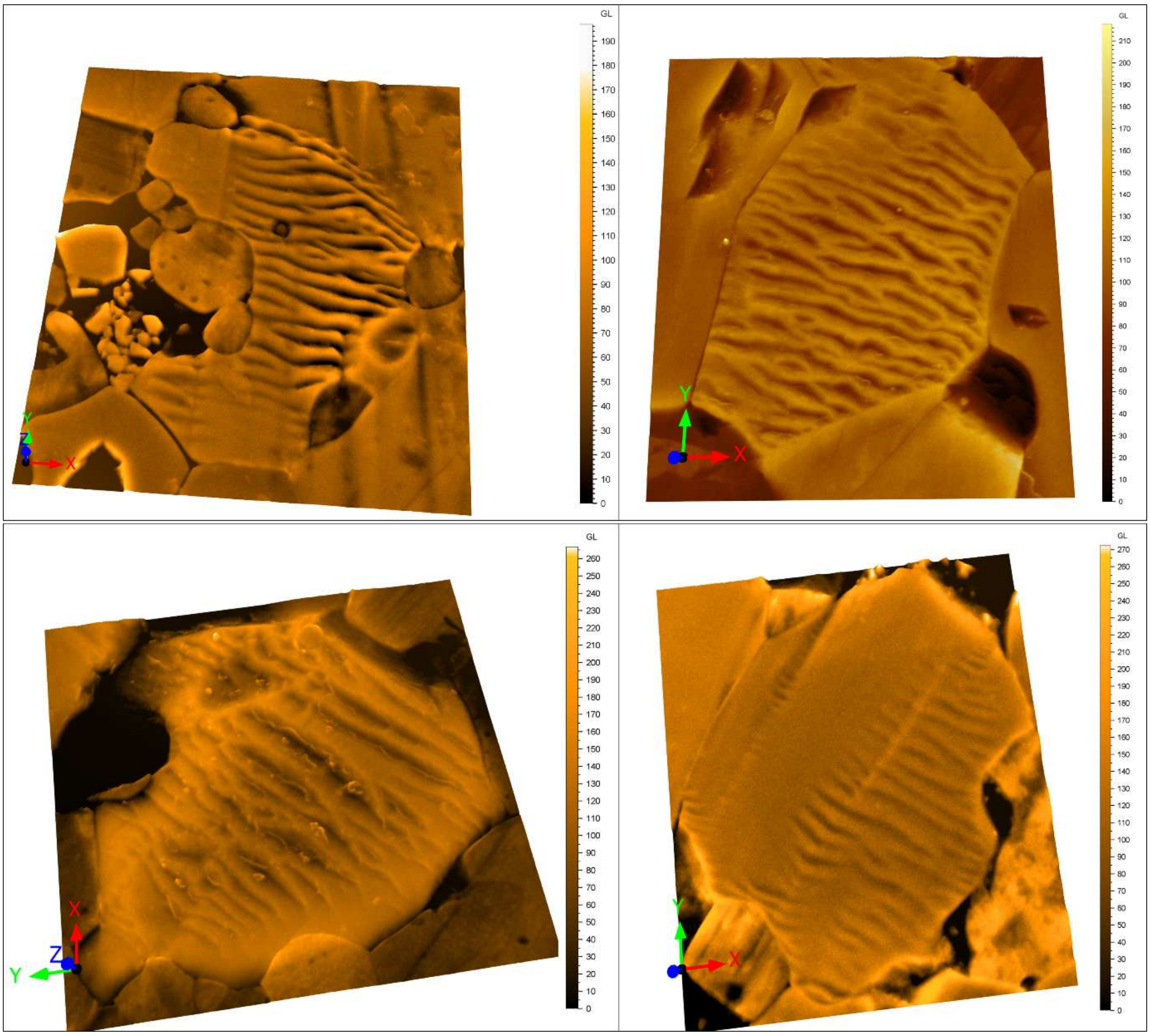

Fig. 20. 3D-SEM reconstruction done on the rippled TiC grains from the wear track of the TiC-50 mol.% SiC composite.

It is noteworthy to mention that similar TiC grain ripplocation was observed in the TiC-30 mol.% SiC composite system. This strengthens the fact the observed TiC grain ripplocation is not a one-off event in the TiC-50 mol.% SiC composite system.

3.8. *TEM analyses of the rippled region*

Focused ion beam (FIB) was used to prepare a cross-sectional TEM specimen containing the buckled TiC region (red box in Fig.17a) inside the wear track. Figure 17 shows the lift-out process for preparing the TEM specimen.

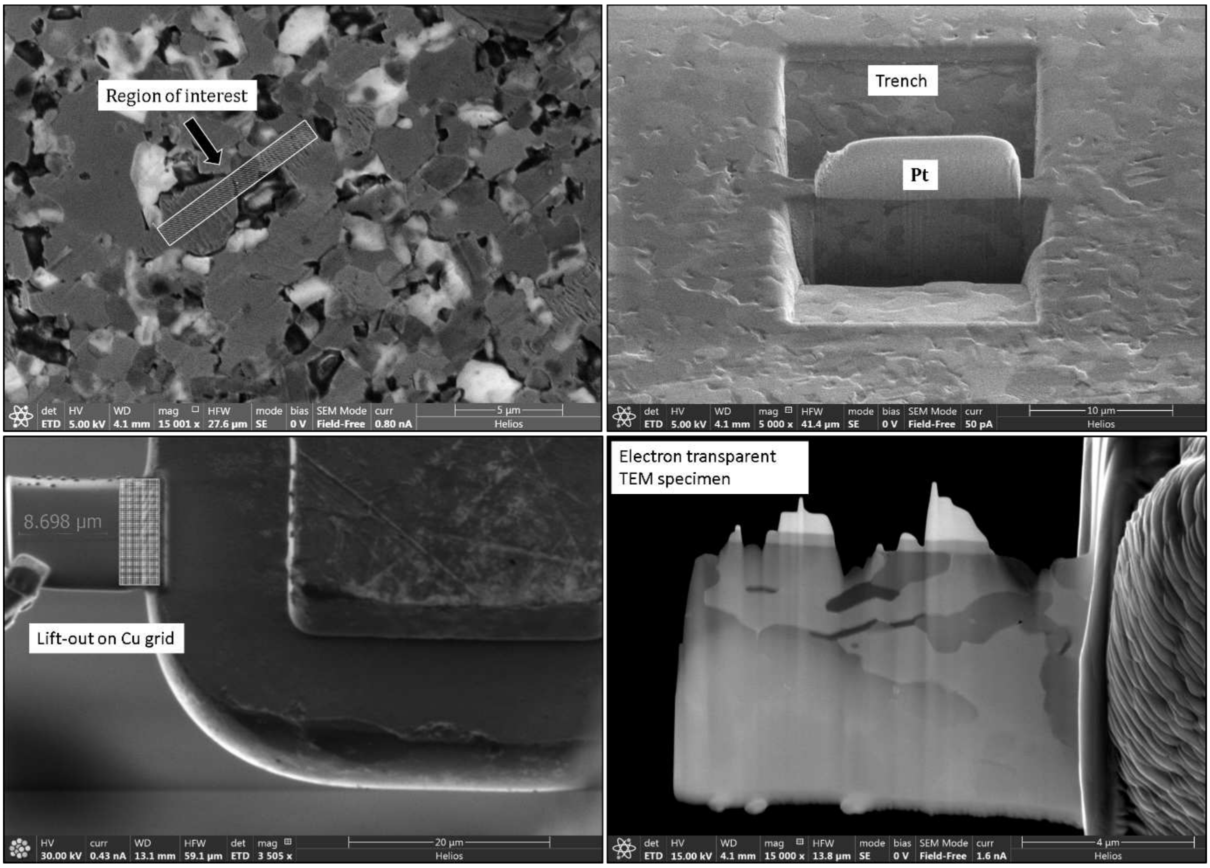

Fig. 21. Ion-induced secondary electron micrographs of FIB sample preparation, showing location where the ripples are extracted from the worn surface and the final electron transparent TEM sample.

Figure 22 shows TEM images taken from the rippled TiC grains. Upon careful observation of the bright-field (BF) TEM images Fig. 22(a) and higher magnification Fig. 22(b), a systematic exfoliation of carbon from the TiC grain was observed. Selected area electron diffraction pattern (SAED) corresponding to region (1), inset in (a), confirms the assignment as graphite with rings matching literature values. Fig. 22(c) shows the HRTEM imaging of the interface position indicated by red rectangle in (b) and corresponding diffraction pattern presented in (d).The diffraction pattern shows graphite rings surrounded by TiC diffraction spots in consistent with the HRTEM imaging of the TiC-graphite interface region.

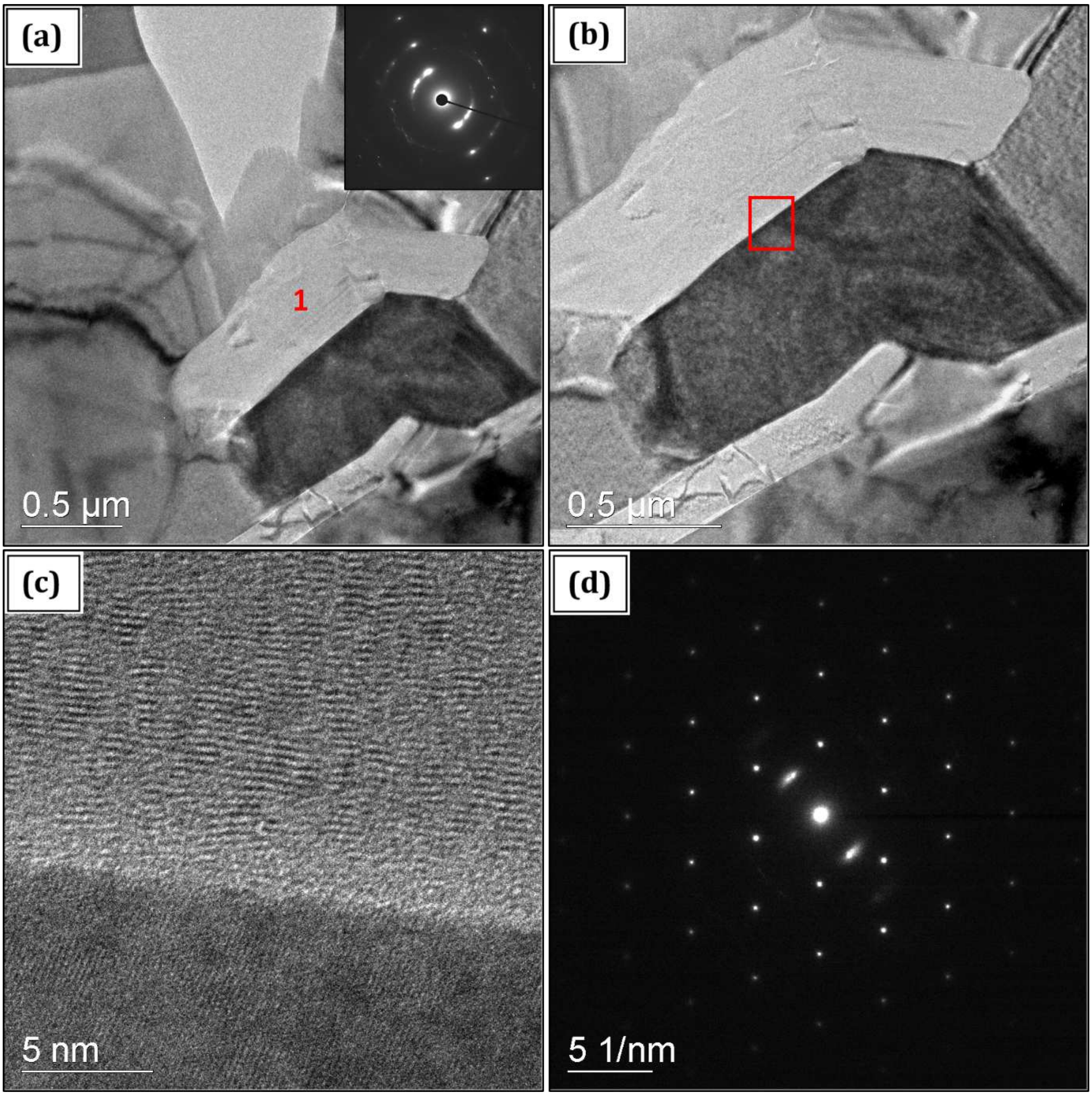

Fig. 22. TEM images taken from the rippled TiC grains showing (a-b) bright-field (BF) images, (c) aberration corrected HRTEM image from the interface (red rectangle in (b)) and (c) corresponding SAED pattern from the interface.

Elemental concentration maps determined by TEM-EDS from the section Fig. 21(a) is presented in Figure 23. The map reveals inward oxygen concentration in areas of TiC depleted of carbon to further highlight the possible systematic mechanical exfoliation of carbon as carbon reach region can be seen from the maps.

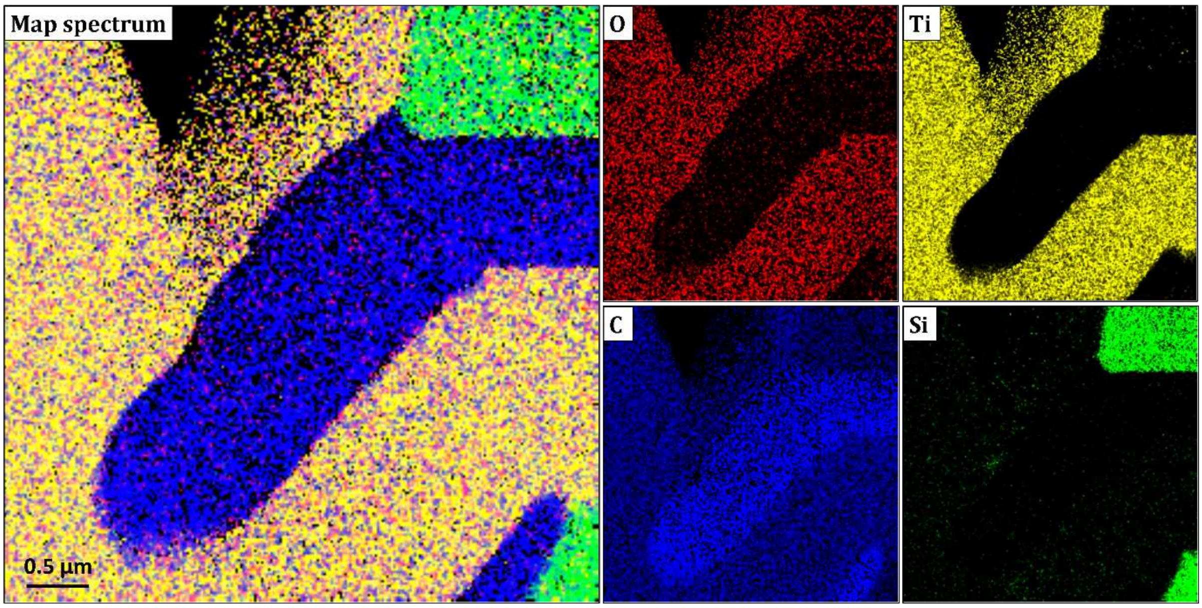

Fig. 23. TEM-EDS elemental concentration map of the rippled TiC grains taken from the wear tracks. All scale bars are 0.5 µm.

The observed ripplocations in the TiC grains is consistent with a new deformation mechanism termed bulk ripplocation (BR) as reported in 2D materials [35]. Recently, layered solids such as graphite, MAX phases, MoS_2 and mica have been reported to deform via a micromechanism involving the nucleation and propagation of ripplocations [35-38]. According to Kushima et al.[35], ripplocation implies surface ripples and crystallographic dislocations and are essentially different to dislocations as such that they possess no Burgers vector or polarity [35, 36]. The formation of ripplocation is essentially associated to an atomic scale buckling which is not restricted to surfaces or near surfaces and can effectively occur in bulk in what was termed bulk ripplocations (BRs) [38].

3.9. Mechanism of ripplocation formation

Superimposition of the shear stresses from the contact sliding load on the inherent tensile residual stresses around the TiC grains will lead to possible weakening of the Ti-C bond, thus the systematic mechanical exfoliation of carbon unto the surface of the TiC grains. The exfoliated carbon then decomposes into graphite due to frictional heating and subsequently deforms via a micromechanism involving the nucleation and propagation of ripplocation as result of the repeated sliding contact. More work needs to be done to fully understand mechanisms leading to the exfoliation of carbon.

4. Wear mechanism

Upon microstructural and chemical characterization of the worn surfaces of the bulk samples, the underlying wear mechanisms are elucidated for this test conditions as follows:

4.1. Tribo-oxidative wear

Tribo-oxidation appears from the Raman analysis to be an operative wear mechanism. The dry sliding nature of the tribological test seems to have generated enough frictional heating due to asperity temperature flashes to trigger selective oxidation of the TiC in both ceramic compositions (i.e., monolithic TiC and TiC-SiC composite). The tribo-oxidatively formed TiO_2 alongside the graphitic layer acts as solid lubricant shielding the interface to prevent direct contact of the tribocouples. In the case of monolithic TiC, 'oxidation-scrape-reoxidation' appears to be taking place very rapidly such that limited contact is made between the tribocouples, thus the limited surface damage observed in sliding surface of TiC/Al_2O_3 tribocouple. For the composite, it seems that the oxidatively formed TiO_2 has a lower fraction as compared to monolithic TiC simply due to the lower volume fraction of TiC in the composition. Since silicon has higher oxidation resistance than titanium, this explains the absence of silicon oxide in the Raman analysis of the composite wear track. The limited TiO_2 formation will then mean that repeated direct contact between the counterparts occurs faster, consistent with the instability in coefficient of friction seen in the $TiC\text{-}SiC/Al_2O_3$ tribocouples.

4.2. Abrasive wear

Abrasive wear was also an operational wear mechanism, this manifest by the evolution of horizontal grooves in the post-mortem sliding surfaces of both the monolithic and composite samples. The wear grooves tends to be more pronounced in the composite sample as compared to the monolithic TiC due to limited TiO_2 tribofilms formed at the sliding surface causing extended contact between the tribocouples. Al_2O_3 fragments transfer material from the ball were however not found in the wear track possibly due to its very low content or the area mapped by EDS and probed by Raman did not contain the transfer material.

4.3. Stress-relaxation induced wear mechanism

The simultaneous influence of the contact stress superimposed on the residual stress initiates the relief of residual stress previously trapped in the composite after sintering during the wear test. The release of residual stresses leads to the weakening of the interface (grain boundary) strength that causes grain pull-outs and microcrack formation. The weakening of the interface enables easy pull-out of the SiC grains which is then subsequently fractured to constitute an abrasive third-body. This will mean that the area in which beneficial compressive stresses prevail decreases, making this toughening mechanism less significant as wear progresses. As a result, detrimental tensile residual stress in the TiC grains will result in the ripplocation of the TiC grains due to the addition shear stresses imposed by the normal contact load. The combination of SiC grain pull-outs due to stress relaxation and TiC grain ripplocation increases the friction coefficient and specific wear rate of the composite system.

5. Conclusion

Monolithic TiC and TiC-SiC composite were successfully synthesized without sintering aids using SPS. The microstructure and tribological properties of the as-sintered samples were studied, and the following conclusions can be drawn:

(1) Mismatch in thermal expansion between TiC and SiC as well as $\beta \rightarrow \alpha$ SiC phase transformation led to high residual stresses in the composite system.
(2) Tribofilms formation due to frictional heating induced tribo-oxidation acts as a protective layer at the disk/ball surface during sliding and reduces friction and wear of the counterparts.
(3) Friction and wear behaviour of the monolithic TiC sample were superior to that of the composite albeit possessing better fracture toughness for the test condition. This is attributed to the incipient stress-relaxation and subsequent SiC grain pull-outs due to the shear stresses imposed upon sliding contact, thus generating abrasive third-body.
(4) Mechanical exfoliation of carbon and its subsequent transformation into graphite due to frictional heating led to the stochastic deformation of the TiC grains via the nucleation of ripplocations.

Future exhaustive characterization will be needed to fully understand the combination of factors leading to the exfoliation of carbon from TiC as this is not fully understood at this time.

References

1. Wei, G.C. and P.F. Becher, Improvements in Mechanical Properties in SiC by the Addition of TiC Particles. Journal of the American Ceramic Society, 1984. **67**(8): p. 571-574.
2. Jiang, D.L., et al., Studies on the strengthening of silicon carbide-based multiphase ceramics I: The SiC-TiC system. Materials Science and Engineering: A, 1989. **109**: p. 401-406.
3. Chen, J., W. Li, and W. Jiang, Characterization of sintered TiC–SiC composites. Ceramics International, 2009. **35**(8): p. 3125-3129.
4. Kawai, C., K. Suzuki, and K. Tanaka, Fracture Toughness of TiC-SiC Composites Fabricated by CVD and the Mechanism of Toughening. Journal of the Ceramic Society of Japan, 1992. **100**(1162): p. 835-840.
5. Ralf Riedel, I.-W.C., Ceramics Science and Technology : Materials and Properties. Vol. Volume 2. 2010: Weinheim : Wiley-VCH.
6. Wäsche, R., et al., Oscillating sliding wear behaviour of SiC, TiC, TiB2, 59SiC–41TiB2 and 52SiC–24TiC–24TiB2 materials up to 750°C in air. Tribotest, 2006. **12**(2): p. 99-111.
7. Ajayi, O.O., et al., Sliding Wear of Silicon Carbide—Titanium Boride Ceramic-Matrix Composite. Journal of the American Ceramic Society, 1993. **76**(2): p. 511-517.
8. H., L.J., et al., Microstructure, Phase and Thermoelastic Properties of Laminated Liquid-Phase-Sintered Silicon Carbide–Titanium Carbide Ceramic Composites. Journal of the American Ceramic Society, 2007. **90**(7): p. 2189-2195.
9. Gille, G. and K. Wetzig, Investigations on mechanical behaviour of brittle wear-resistant coatings I. Experimental results. Thin Solid Films, 1983. **110**(1): p. 37-54.
10. Magnus, C., T. Kwamman, and W.M. Rainforth, Dry sliding friction and wear behaviour of TiC-based ceramics and consequent effect of the evolution of grain buckling on wear mechanism. Wear, 2019. **422-423**: p. 54-67.
11. Srivatsan, T.S., et al., Influence of TiB2 content on microstructure and hardness of TiB2–B4C composite. Powder Technology, 2005. **159**(3): p. 161-167.
12. King, D.S., W.G. Fahrenholtz, and G.E. Hilmas, Silicon carbide–titanium diboride ceramic composites. Journal of the European Ceramic Society, 2013. **33**(15): p. 2943-2951.
13. Sowmya, A. and C.A. H., Synthesis of Titanium Silicon Carbide. Journal of the American Ceramic Society, 1995. **78**(3): p. 667-672.
14. Kim, Y.W., et al., Effect of Initial α-Phase Content on Microstructure and Mechanical Properties of Sintered Silicon Carbide. Journal of the American Ceramic Society, 1998. **81**(12): p. 3136-3140.
15. H. McMurtry, C., et al., Microstructure and Material Properties of SiC-TiB2 Particulate Composite. Vol. 66. 1987. 325-329.
16. Woydt, M., A. Skopp, and K.H. Habig, Dry friction and wear of self-mated sliding couples of SiC-TiC and Si3N4-TiN. Wear, 1991. **148**(2): p. 377-394.
17. Wäsche, R. and D. Klaffke, In situ formation of tribologically effective oxide interfaces in SiC-based ceramics during dry oscillating sliding. Tribology Letters, 1998. **5**(2): p. 173.
18. Brüesch, P., Phonons: theory and experiments. 2, Experiments and interpretation of experimental results. 1986, London: Springer-Verlag.
19. Huong, P.V., Structural studies of diamond films and ultrahard materials by Raman and micro-Raman spectroscopies. Diamond and Related Materials, 1991. **1**(1): p. 33-41.
20. Klein, M.V., J.A. Holy, and W.S. Williams, Raman scattering induced by carbon vacancies in TiCx. Physical Review B, 1978. **17**(4): p. 1546-1556.
21. Balachandran, U. and N.G. Eror, Raman spectra of titanium dioxide. Journal of Solid State Chemistry, 1982. **42**(3): p. 276-282.

22. Tuinstra, F. and J.L. Koenig, Raman Spectrum of Graphite. The Journal of Chemical Physics, 1970. **53**(3): p. 1126-1130.
23. Pang, W.K., et al., 12 - Oxidation characteristics of Ti3AlC2, Ti3SiC2 and Ti2AlC, in Advances in Science and Technology of Mn+1AXn Phases. 2012, Woodhead Publishing. p. 289-322.
24. Kim, Y.-W., S.-G. Lee, and Y.-I. Lee, Pressureless Sintering of SiC–TiC Composites with Improved Fracture Toughness. Vol. 35. 2000. 5569-5574.
25. Ahmoye, D., Pressureless Sintering and Mechanical Properties of SiCComposites with in-situ Converted TiO2 to TiC, in Department of Mechanical and Materials Engineering. 2010, Queen's University Kingston, Ontario, Canada.
26. Endo, H., M. Ueki, and H. Kubo, Microstructure and mechanical properties of hot-pressed SiC-TiC composites. Journal of Materials Science, 1991. **26**(14): p. 3769-3774.
27. Kornaus, K., et al., Mechanical properties of hot-pressed SiC-TiC composites. Vol. 11. 2017. 329-336.
28. Qin, C., et al., Microstructure Characterization and Mechanical Properties of TiSi2-SiC-Ti3SiC2 Composites Prepared by Spark Plasma Sintering. Vol. 47. 2006. 845-848.
29. Gu, W.H. and K.T. Faber, Tensile behavior of microcracking SiC-TiB$_2$ composites. Journal of the American Ceramic Society, 1995. **78**(6): p. 1507-1512.
30. Magley, D., R. Winholtz, and K. Faber, Residual Stresses in a Two-Phase Microcracking Ceramic. J. Am. Ceram. Soc, 1990. **73**(6): p. 1641-1644.
31. Luan, W., C. Jiang, and V. Ji, Residual Stress Relaxation in Shot Peened Surface Layer on TiB2/Al Composite under Applied Loading. MATERIALS TRANSACTIONS, 2009. **50**(1): p. 158-160.
32. J., G.D., Stress-Induced Microcracking at Second-Phase Inclusions. Journal of the American Ceramic Society, 1981. **64**(3): p. 138-141.
33. Evans, A.G. and Y. Fu, Some effects of microcracks on the mechanical properties of brittle solids—II. Microcrack toughening. Acta Metallurgica, 1985. **33**(8): p. 1525-1531.
34. Evans, A.G. and K.T. Faber, Toughening of Ceramics by Circumferential Microcracking. Journal of the American Ceramic Society, 1981. **64**(7): p. 394-398.
35. Kushima, A., et al., Ripplocations in van der Waals Layers. Nano Letters, 2015. **15**(2): p. 1302-1308.
36. Gruber, J., et al., Evidence for Bulk Ripplocations in Layered Solids. Scientific Reports, 2016. **6**: p. 33451.
37. Barsoum, M.W., et al., Ripplocations: A universal deformation mechanism in layered solids. Physical Review Materials, 2019. **3**(1): p. 013602.
38. Griggs, J., et al., Spherical nanoindentation, modeling and transmission electron microscopy evidence for ripplocations in Ti3SiC2. Acta Materialia, 2017. **131**: p. 141-155.